# Tumor cell–intrinsic EPHA2 suppresses antitumor immunity by regulating PTGS2 (COX-2)

Nune Markosyan,[1] Jinyang Li,[2] Yu H. Sun,[3] Lee P. Richman,[2] Jeffrey H. Lin,[2] Fangxue Yan,[2] Liz Quinones,[2] Yogev Sela,[2] Taiji Yamazoe,[2] Naomi Gordon,[2] John W. Tobias,[4] Katelyn T. Byrne,[1,5] Andrew J. Rech,[2,5] Garret A. FitzGerald,[6,7] Ben Z. Stanger,[1,2,5,8,9] and Robert H. Vonderheide,[1,2,5,9,10]

[1]Department of Medicine, [2]Abramson Family Cancer Research Institute, [3]Center for RNA Biology, Department of Biochemistry and Biophysics, Department of Urology, University of Rochester Medical Center, Rochester, New York, USA. [4]Penn Genomic Analysis Core, [5]Parker Institute for Cancer Immunotherapy, [6]Department of Systems Pharmacology and Translational Therapeutics, [7]Institute for Translational Medicine and Therapeutics, [8]Department of Cell and Developmental Biology, [9]Abramson Cancer Center, and [10]Institute for Immunology, University of Pennsylvania, Philadelphia, Pennsylvania, USA.

**Resistance to immunotherapy is one of the biggest problems of current oncotherapeutics. While T cell abundance is essential for tumor responsiveness to immunotherapy, factors that define the T cell–inflamed tumor microenvironment are not fully understood. We used an unbiased approach to identify tumor-intrinsic mechanisms shaping the immune tumor microenvironment (TME), focusing on pancreatic adenocarcinoma because it is refractory to immunotherapy and excludes T cells from the TME. From human tumors, we identified ephrin-A receptor 2 (EPHA2) as a candidate tumor-intrinsic driver of immunosuppression. *Epha2* deletion reversed T cell exclusion and sensitized tumors to immunotherapy. We found that prostaglandin endoperoxide synthase 2 (*PTGS2*), the gene encoding cyclooxygenase-2, lies downstream of EPHA2 signaling through TGF-β and is associated with poor patient survival. *Ptgs2* deletion reversed T cell exclusion and sensitized tumors to immunotherapy; pharmacological inhibition of PTGS2 was similarly effective. Thus, EPHA2/PTGS2 signaling in tumor cells regulates tumor immune phenotypes; blockade may represent a therapeutic avenue for immunotherapy-refractory cancers. Our findings warrant clinical trials testing the effectiveness of therapies combining EPHA2/TGF-β/PTGS2 pathway inhibitors with antitumor immunotherapy and may change the treatment of notoriously therapy-resistant pancreatic adenocarcinoma.**

## Introduction

Immunotherapies, including immune checkpoint blockade (ICB), have led to significant improvement of clinical care for cancer patients (1–4). Patients with melanoma, lung adenocarcinoma, or kidney cancer have a 20%–40% response rate to ICB (5). Unfortunately, the majority of patients with these and other types of cancer remain refractory to ICB. One key determinant of sensitivity to immunotherapies is the abundance of tumor-infiltrating $CD8^+$ T cells (6), and tumors can be stratified into T cell–inflamed or non–T cell–inflamed tumors based on the degree of T cell infiltration (7). Importantly, non–T cell–inflamed tumors appear to have decreased sensitivity to immunotherapies compared with T cell–inflamed tumors across human cancer, a concept we recently modeled in genetically engineered mice (8, 9). Thus, there is an urgent need to understand how T cell infiltration is controlled in tumors.

Pancreatic ductal adenocarcinoma (PDA) is predicted to become the second leading cause of cancer-related death and is largely refractory to existing therapeutic interventions, including immunotherapies (10), primarily due to the immunosuppressive tumor microenvironment (TME) and minimal T cell infiltration in PDA (8, 11, 12). Importantly, we and others found that neither mutational load nor number of predicted neoantigens accounted for variation in the abundance of tumor-infiltrating T cells (9, 13, 14). Instead, recent work has pointed to the critical importance of tumor cell–intrinsic factors — secreted factors, signaling pathways, and epigenetic status — in shaping the tumor immune microenvironment in both PDA (8, 11, 12, 15, 16) and other tumor types (17–22). One important conclusion from these studies is that multiple mechanisms contribute to the heterogeneity of immune infiltration.

In preclinical studies, we demonstrated the efficacy of a combination therapy, including chemotherapy, agonistic CD40, and ICB, in a genetically engineered mouse model of PDA (23, 24). Similarly to what occurred with patients, only some mouse PDA tumors responded well to the combination immunotherapy, while others were resistant; importantly, the abundance of tumor-infiltrating activated $CD8^+$ T cells predicted the sensitivity to therapy (8). These studies provide a rationale for identifying factors that augment the intratumoral presence of activated $CD8^+$ T cells, thereby synergizing with immunotherapy and improving the clinical outcome of PDA.

▶ Related Commentary: p. 3521

**Authorship note:** NM and JL contributed equally to this work.
**Conflict of interest:** RHV reports receiving consulting fees or honoraria from Apexigen, AstraZeneca, Celgene, Genentech, Janssen, Lilly, MedImmune, Merck, and Verastem Oncology; he has received research funding from Apexigen, FibroGen, Inovio, Janssen, and Lilly. BZS has received research funding from Boehringer Ingelheim. GAF is a senior advisor to Calico and has received consulting fees from Amgen, Tremeau Pharmaceuticals, and Heron Therapeutics. He is co-chief scientific advisor to Science Translational Medicine.

**Submitted:** January 26, 2019; **Accepted:** May 29, 2019; **Published:** July 29, 2019.
**Reference information:** *J Clin Invest*. 2019;129(9):3594–3609.
https://doi.org/10.1172/JCI127755.

In this study, we took an unbiased approach to identifying tumor cell–intrinsic factors that shape the immune TME. We found that the expression of ephrin-A receptor 2 (*EPHA2*), a member of the EPH family of receptor tyrosine kinases, is negatively correlated with the degree of T cell infiltration in PDA and that deletion of *EphA2* in tumor cells resulted in an increase in T cell infiltration and conferred sensitivity to immunotherapy. Mechanistically, we found that these effects were mediated through EPHA2/TGF-β/SMAD axis–dependent activation of prostaglandin endoperoxide synthase 2 (*Ptgs2*). The PTGS2 protein encoded by this gene is a potent proinflammatory enzyme known colloquially as cyclooxygenase 2 (COX-2). These results provide a basis for targeting immunosuppressive signals arising from the tumor cells as a sensitization strategy for successful immunotherapy.

## Results

*Expression of EPHA2 inversely correlates with CD8⁺ T cell infiltration in PDA*. To reveal signaling pathways that may suppress the infiltration of CD8⁺ T cells in PDA, we identified 742 genes whose expression correlated inversely with *CD8A* transcript abundance in The Cancer Genome Atlas (TCGA) data set (Figure 1A). Pathway analysis of this group of genes indicated activation of EPH/ephrin signaling as one of the top 5 gene signatures associated with the T cell–noninflamed phenotype (Supplemental Figure 1A and Figure 1B) and identified *EPHA2* as the most highly expressed EPH family member in human PDA (Figure 1C). EPH proteins are a highly conserved family of receptor tyrosine kinases that function in development, particularly in neurogenesis and angiogenesis, and regulate a pleiotropic set of cellular functions. EPHA2 is overexpressed in multiple tumor types, and its expression correlates with poor prognosis and therapy resistance (25). Importantly, the mRNA expression level of *EPHA2* negatively correlated with *CD8A*, *CD3*, *PRF1*, and *GZMB*, but not *IFNG*, in 2 independent data sets of human PDA samples (Figure 1D and Supplemental Figure 1, B and C). Moreover, *EPHA2* expression was inversely correlated with patient survival (Figure 1E), consistent with previous studies showing that a high abundance of tumor-infiltrating T cells is associated with survival in human PDA (26–28). These results suggest that *EPHA2* expression inversely correlates with T cell infiltration in human PDA and may have clinical significance.

We recently reported a library of congenic pancreatic tumor cell clones that faithfully recapitulate the heterogeneity of immune cell infiltration in PDA (8). Specifically, clones fell into 2 categories: T cell–high tumor cell clones, which generate implanted tumors with tumor-infiltrating T cells and a paucity of suppressive myeloid cells, and T cell–low tumor cell clones, which generate tumors with the opposite representation of immune cells (Supplemental Figure 1D). In this experimental system, *Epha2* was again the top expressed gene in the *Eph* family (Figure 1F), and it was expressed predominantly in tumor cells (marked by yellow fluorescent protein [YFP]) as compared with YFP-negative nontumor cells (Figure 1G). Moreover, *Epha2* mRNA and the proportion of EPHA2⁺ cells were higher in subcutaneous tumors derived from T cell–low tumor cells versus T cell–high tumor cells (Figure 1, H and I). Based on this strong correlation between EPHA2 expression and a paucity of tumor-infiltrating CD8⁺ cells in both murine and human PDA, we hypothesized that EPHA2, expressed by cancer cells, regulates immune infiltration in pancreatic cancer.

*Tumor cell–intrinsic Epha2 regulates T cell infiltration and sensitivity to immunotherapy*. To test this hypothesis, we investigated the effect of *Epha2* deletion on the TME using our congenic mouse PDA tumor cell clones. Utilizing the CRIPSR-Cas9 technique, we generated *Epha2*-KO tumor cells from 2 T cell–low tumor cell clones, 6419c5 and 6694c2 (*Epha2*-WT) (Supplemental Figure 2, A and B). *Epha2* ablation in these clones resulted in a significant increase in CD3⁺ T cells in subcutaneously implanted tumors, both in terms of absolute numbers and as a percentage of CD45⁺ cells (Figure 2, A–C). Flow analysis showed that *Epha2*-KO tumors had increased proportions of total and activated CD8⁺ T cells, total CD4⁺ T cells, and further subsets (Figure 2, C–E), but decreased proportions of total myeloid cells and granulocytic myeloid-derived suppressor cells (gMDSCs, Figure 2F). Moreover, *Epha2*-KO tumors had increased CD8⁺/myeloid cell ratios (Supplemental Figure 2C), but no change in the number of macrophages or dendritic cells (Supplemental Figure 2D). We confirmed these results in orthotopically implanted tumors (Figure 2, G and H, and Supplemental Figure 2, E and F). The immunosuppressive character of gMDSCs in this model was shown by functional assays in our previous studies (11, 29). We confirmed by flow cytometry that in *Epha2*-KO tumors, the gMDSCs and macrophages exhibit a phenotype consistent with immunosuppressive function (Supplemental Figure 2, G and H). Interestingly, the expression of fibroblast marker PDGFRβ, but not α–smooth muscle actin (αSMA), was increased in *Epha2*-KO tumors (Supplemental Figure 2I). In addition, the proportions of Ki67-expressing YFP⁺ tumor cells and tumor weights were decreased in *Epha2*-KO tumors (Supplemental Figure 2, J–L). These results indicate that *Epha2* expression by pancreatic cancer cells promotes the establishment of an immune TME dominated by myeloid cells and a paucity of tumor-infiltrating T cells.

We recently demonstrated that, compared with T cell–high tumors, T cell–low tumors have decreased sensitivity to a combination of chemo- and immunotherapy, GAFCP (gemcitabine [G], nab-paclitaxel [A], anti-CD40 agonist [F], anti–CTLA-4 [C], and anti–PD1-1 [P]; refs. 8, 23, 24). Given that *Epha2* KO converted parental (T cell–low) tumors to the T cell–inflamed phenotype, we then tested *Epha2* KO tumor sensitivity to the combination therapy. Ablation of *Epha2* in cancer cells significantly improved the therapeutic efficacy of GAFCP with respect to tumor growth and overall survival (Figure 3, A–C). Collectively, these experiments suggest that EPHA2 expression in cancer cells promotes an immunosuppressive TME that confers resistance to combination immunotherapy.

*Transcriptional profiling identifies Ptgs2 as a potential tumor cell–intrinsic regulator of the TME*. To identify tumor cell–intrinsic factors mediating these *Epha2*-dependent phenotypes, we performed RNA-Seq and differential gene expression analysis of sorted tumor cells from subcutaneously implanted *Epha2*-WT and *Epha2*-KO tumors (Figure 4A). Gene set enrichment analysis (GSEA) revealed that *Epha2*-KO tumors exhibit a signature of IFN response and inflammatory pathways, similar to gene signatures observed in T cell–high tumor cells (Supplemental Figure 3, A and B, and ref. 8). Immunostaining for STAT1 confirmed the activation of IFN signaling pathways in *Epha2*-KO tumors (Supplemental Figure 3C).

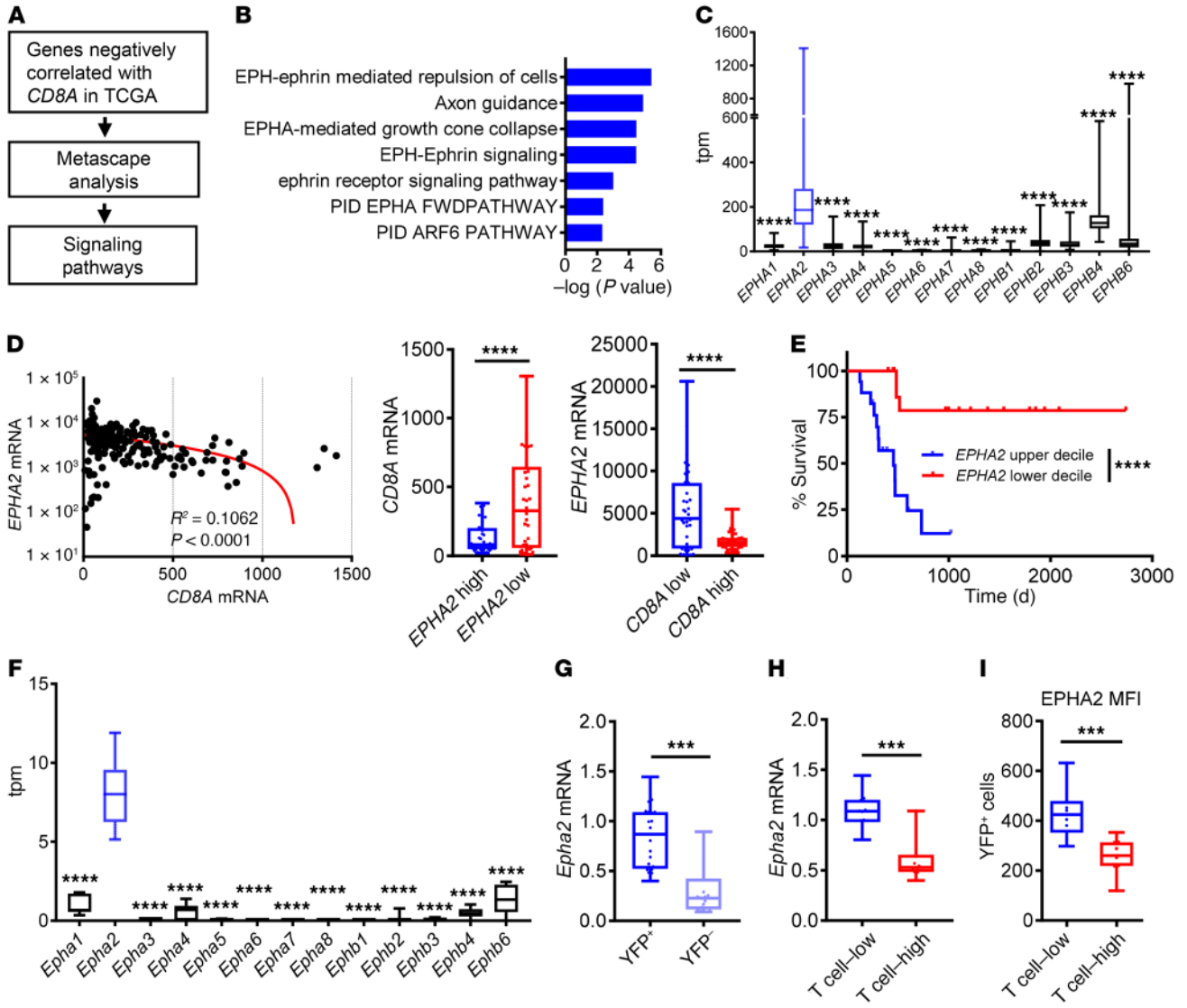


**Figure 1. Expression of *EPHA2* correlates with the abundance of CD8⁺ T cells in PDA.** (**A**) Pipeline for identification of signaling pathways negatively associated with the abundance of *CD8A* transcripts in the TCGA PDA data set. (**B**) EPH-ephrin signaling pathways inversely correlated with *CD8A* transcript abundance in TCGA PDA data set. (**C**) The transcript abundance of EPH receptor family members in human PDA data set from TCGA. (**D**) Correlation of transcript abundance for *CD8A* and *EPHA2* in human PDA samples from TCGA (left). Abundance of *CD8A* transcript in the top and bottom 20% of *EPHA2* expression (middle), and *EPHA2* transcript abundance in top and bottom 20% of *CD8A* expression (right) in human PDA samples from TCGA. (**E**) Kaplan-Meier survival curves generated from TCGA PDA data set; upper and lower deciles of *EPHA2* expression presented ($n$ = 17/group). (**F**) The transcript abundance of EPH receptor family members in mouse PDA cells ($n$ = 7/group). (**G**) The mRNA expression levels of *Epha2* in YFP⁺ tumor cells and YFP⁻ stromal cells from subcutaneously implanted KPCY tumors ($n$ = 20/group). (**H**) The mRNA expression levels of *Epha2* in YFP⁺ tumor cells from subcutaneously implanted mouse T cell–high and T cell–low KPCY tumors ($n$ = 10/group). (**I**) The surface protein levels of Epha2 in YFP⁺ tumor cells from subcutaneously implanted T cell–high and T cell–low KPCY tumors ($n$ = 10/group). (**C**, **D**, **F**–**I**) Data are presented as box plots; each symbol represents a single patient or mouse tumor sample, and each box represents a group with horizontal lines and error bars indicating mean and range, respectively. Statistical analysis by Students' unpaired $t$ test (**D**, **G**–**I**) or 1-way ANOVA with Tukey's HSD post test (**C** and **F**). ***$P < 0.001$; ****$P < 0.0001$.

In addition, *Epha2*-KO tumors had increased expression of antigen presentation genes, including MHC I, on the tumor cells in vivo (Supplemental Figure 3, D and E). However, when treated with IFNs in vitro, *Epha2*-KO tumor cells failed to express increased levels of MHC I compared with untreated controls, suggesting that increased antigen presentation by *Epha2*-KO cells requires an input from the TME (Supplemental Figure 3F).

We previously demonstrated that in T cell–low tumors, cancer cells actively suppress the local immune response. Thus, we focused on the genes enriched in both *Epha2*-WT tumor cells (compared with *Epha2*-KO) and T cell–low tumor cell clones (compared with T cell–high tumor cell clones) to identify candidate tumor cell–intrinsic factors. This approach yielded 17 genes that were expressed by tumor cells and significantly associated with an immunosuppressed TME in both T cell–low tumor cell lines (Figure 4, B and C, and not shown). Furthermore, we performed differential gene expression analysis of human T cell–low and T cell–high PDA tumors based on the top and bottom 20% expres-

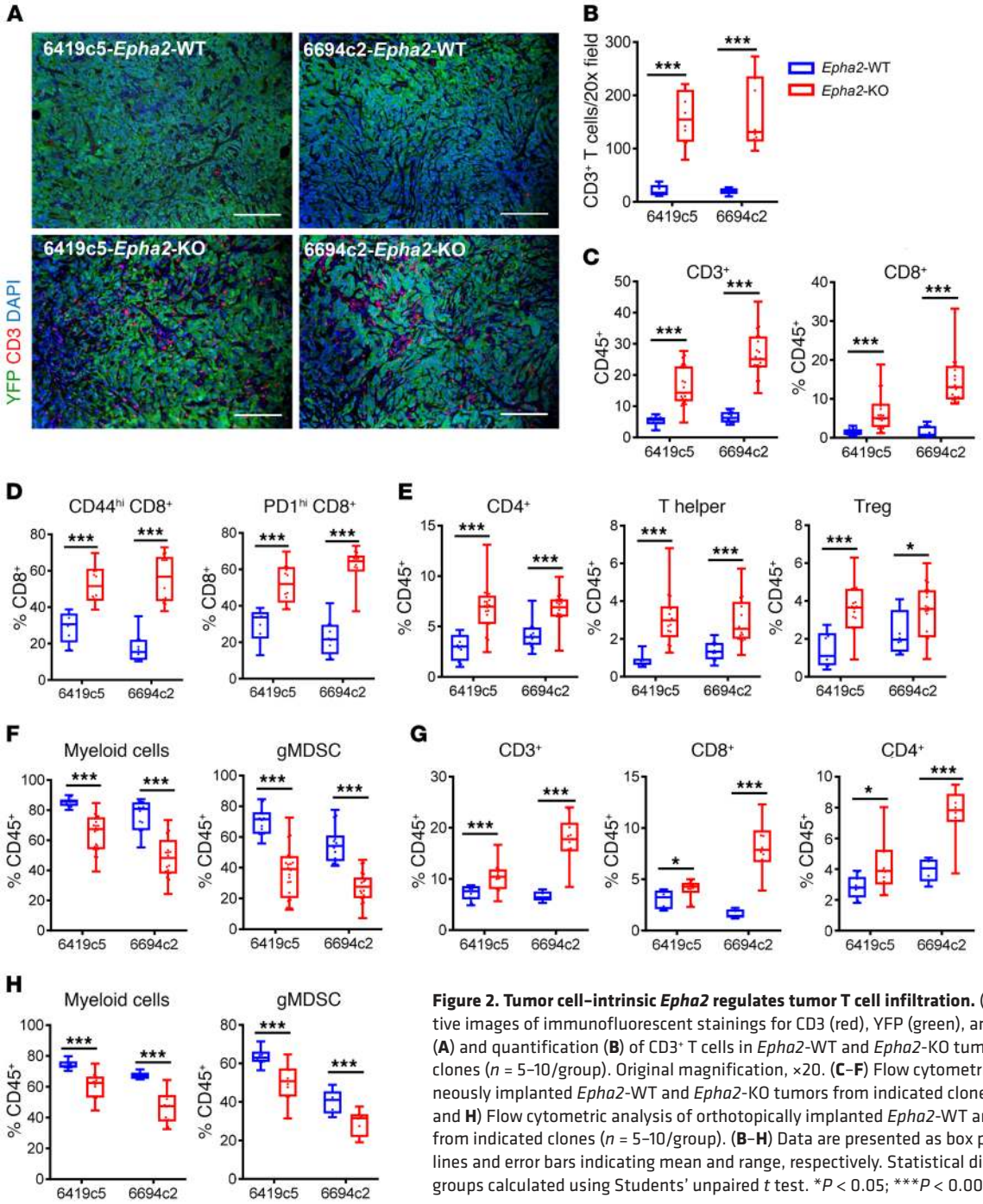


**Figure 2. Tumor cell–intrinsic *Epha2* regulates tumor T cell infiltration.** (**A** and **B**) Representative images of immunofluorescent stainings for CD3 (red), YFP (green), and nuclei (DAPI, blue) (**A**) and quantification (**B**) of CD3+ T cells in *Epha2*-WT and *Epha2*-KO tumors from indicated clones ($n$ = 5–10/group). Original magnification, ×20. (**C**–**F**) Flow cytometric analysis of subcutaneously implanted *Epha2*-WT and *Epha2*-KO tumors from indicated clones ($n$ = 12–25/group). (**G** and **H**) Flow cytometric analysis of orthotopically implanted *Epha2*-WT and *Epha2*-KO tumors from indicated clones ($n$ = 5–10/group). (**B**–**H**) Data are presented as box plots, with horizontal lines and error bars indicating mean and range, respectively. Statistical differences between groups calculated using Students' unpaired $t$ test. *$P$ < 0.05; ***$P$ < 0.001.

sion of *CD8A* and found that 3 of these 17 genes — *CCK*, *MACC1*, and *PTGS2* — were also significantly enriched in human T cell–low tumor samples (Supplemental Figure 3G). Among these 3 genes, *Ptgs2* was the most highly expressed gene in sorted T cell–low tumor cells from implanted mouse T cell–low tumors (base mean = 2189.05; Figure 4D), compared with the other 2 genes (*Cck* base mean = 15.3051, *Macc1* base mean = 56.7993). While *PTGS2* expression was not different between T cell cytolytic activity–high and –low human PDA samples (Figure 4E), patients with *PTGS2* expression in the lower decile had significantly improved survival (Figure 4F). These results suggest that *PTGS2* expression correlates with a T cell–low tumor phenotype and improved survival across species.

TGF-β signaling has been reported to regulate *PTGS2* expression in tumors (30, 31). Hypergeometric Optimization of Motif EnRichment (HOMER) analysis predicted SMAD3 as one of the top transcriptional regulators in *Epha2*-WT tumor cells (Figure 4G), and GSEA analysis revealed a TGF-β signaling signature as greatly depleted in *Epha2*-KO tumor cells (Figure 4H), raising the possibility that TGF-β signaling regulates *Ptgs2* expression in our murine tumor system. To test this possibility, we first exposed murine PDA tumor cells to TGF-β in vitro,

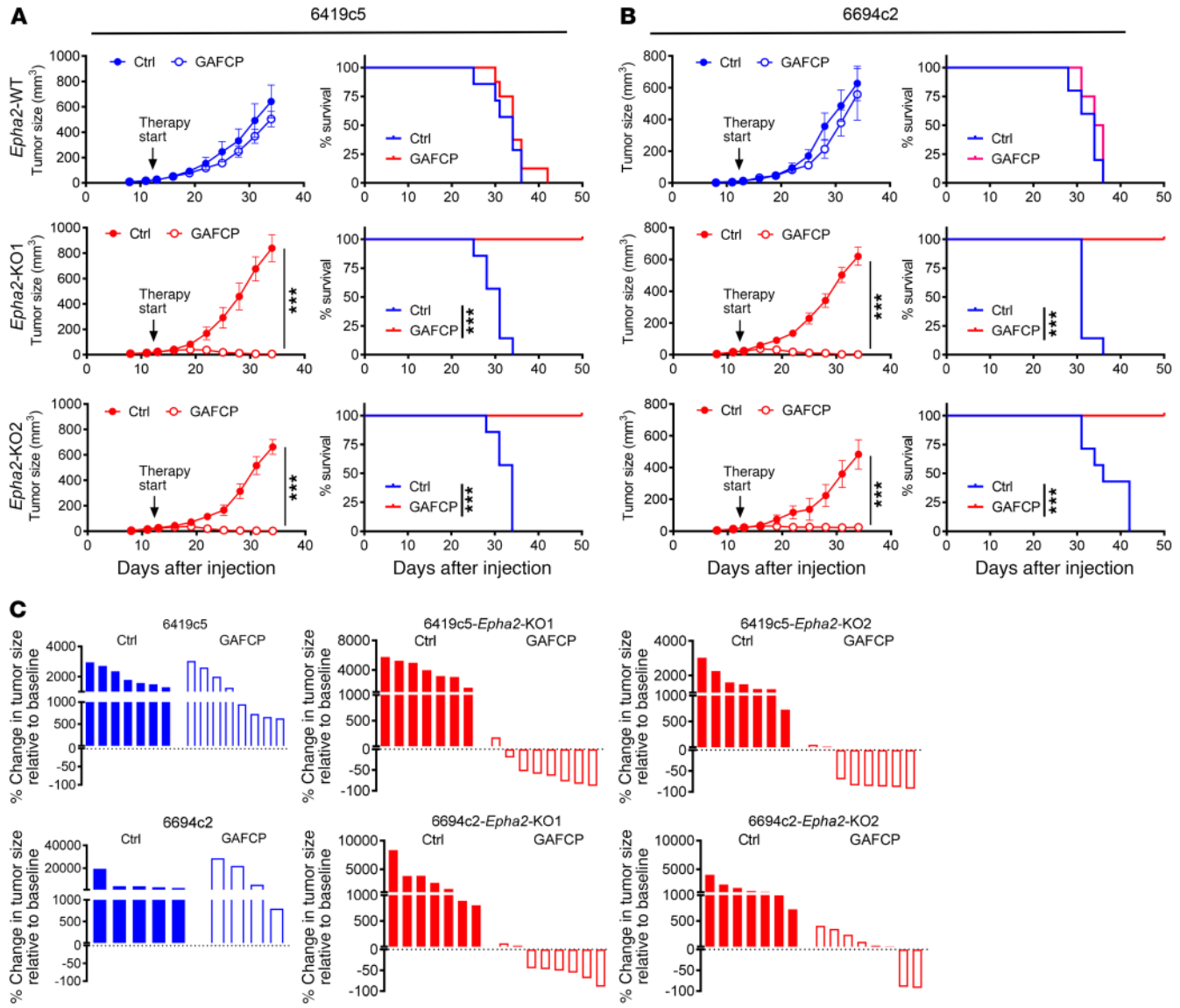


**Figure 3. Tumor cell–intrinsic *Epha2* regulates sensitivity to immunotherapy.** (**A** and **B**) *Epha2*-WT and *Epha2*-KO tumor growth and mouse survival with or without the GAFCP treatment. Tumor cells implanted subcutaneously into C57BL/6 mice ($n$ = 4–8/group). GAFCP treatment started 12 days after implantation, at 3–5 mm tumor diameter. (**C**) Size change of *Epha2*-WT and *Epha2*-KO tumors from indicated clones relative to the baseline after 3 weeks with or without GAFCP treatment. PDA tumor cells were implanted subcutaneously into C57BL/6 mice ($n$ = 4–8/group) and treated with GAFCP for 12 days (average tumor diameter 3–5 mm at the treatment start). Statistical differences between groups calculated by linear mixed-effects model with Tukey's HSD post test using the lme4 in R (**A** and **B**, left). The log-rank $P$ values for Kaplan-Meier survival curves were calculated in GraphPad Prism (**A** and **B**, right). ***$P < 0.001$.

which uniformly resulted in an upregulation of *Ptgs2* (Figure 4I). Next, we performed CRISPR-Cas9–mediated KO of *Smad3* or *Smad4* in a T cell–low tumor clone (Supplemental Figure 3H). This resulted in a significant decrease in the expression of *Ptgs2* (Figure 4J) and a corresponding change in T cell and myeloid populations following subcutaneous implantation (Figure 4, K and L), consistent with a conversion to a T cell–high (or *Epha2*-KO) phenotype. Interestingly, TGF-β treatment also led to an increase in the cell-surface expression of EPHA2 (Supplemental Figure 3I), while *Smad3* or *Smad4* KO led to a decrease in EPHA2 expression in vitro and in vivo (Supplemental Figure 3, J and K), suggesting that a positive feedback loop may regulate EPHA2 levels. Collectively, these data suggest that EPHA2-mediated modulation of TME occurs through TGF-β/SMAD3–dependent regulation of PTGS2.

*Mice with a pancreas-specific deletion of Ptgs2 have suppressed tumor growth.* To investigate the role of PTGS2 in PDA in its anatomical niche, we next engineered a biallelic deletion of *Ptgs2* in the pancreatic epithelial cells of KPCY mice using homozygous floxed *Ptgs2* alleles (KPCY$^{PTGS2}$, Figure 5A). KPCY mice recapitulate salient features of human PDA, including the molecular, clinical, and histological features of disease, with 100% penetrance (31). We confirmed loss of *Ptgs2* expression in the epithelial cells of KPCY$^{Ptgs2}$ mice by immunohistochemistry (Figure 5B) and then followed cohorts of KPCY and KPCY$^{Ptgs2}$ mice clinically and by ultrasound, comparing tumor onset and overall survival (Figure

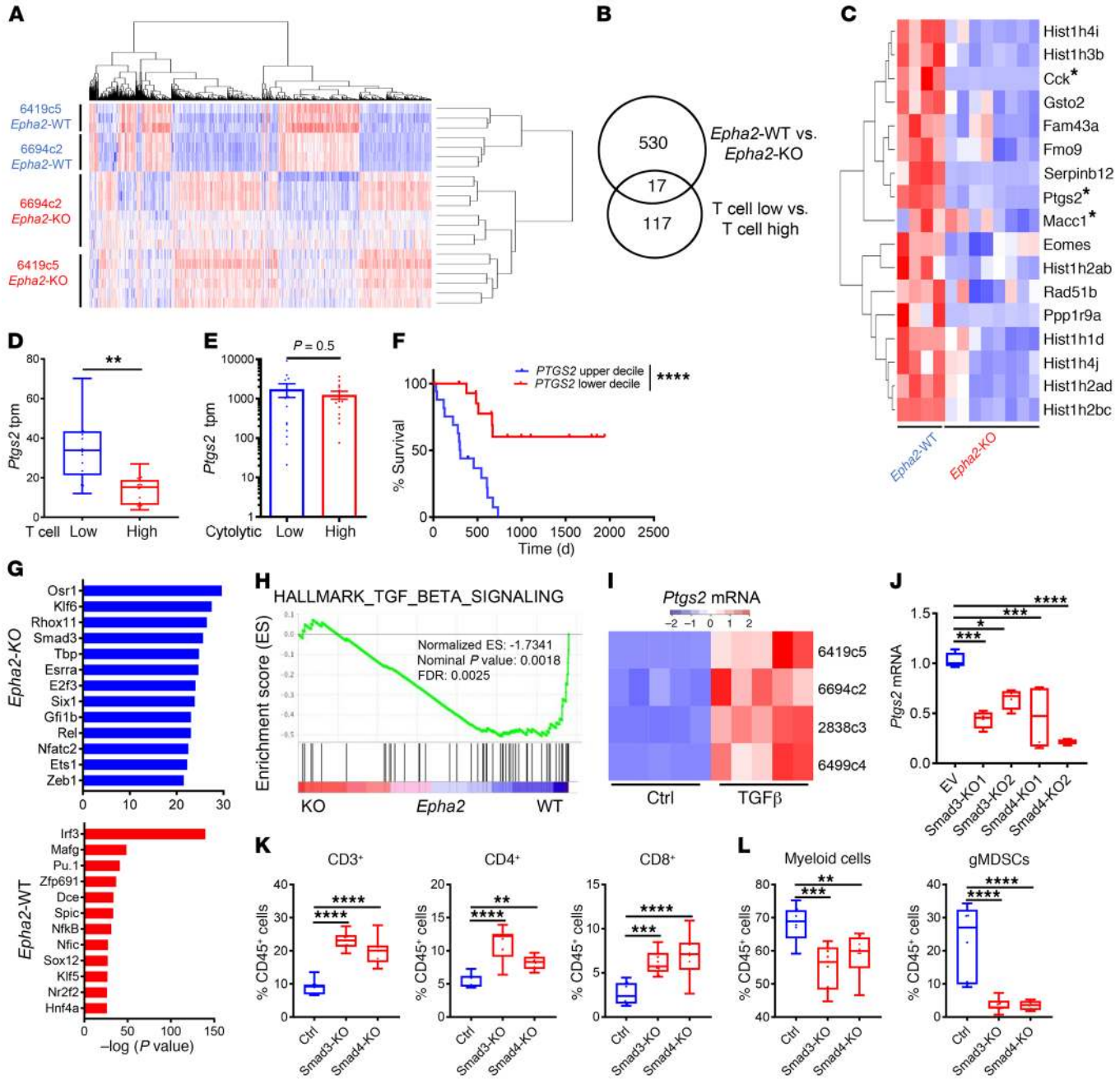


**Figure 4. PTGS2 is a potential tumor cell–intrinsic regulator of TME.** (**A**) Heatmap of differentially expressed genes in *Epha2*-WT and *Epha2*-KO tumor cells from subcutaneously implanted tumors from indicated clones ($n$ = 3–8/group). (**B**) Overlap of the genes enriched in *Epha2*-WT (vs. *Epha2*-KO) and T cell–low (vs. T cell–high) tumors. (**C**) Seventeen coenriched genes identified (**B**) in *Epha2*-WT and *Epha2*-KO tumor cells from subcutaneously implanted mouse tumors (clone 6694c2). (**D**) Boxplot of *Ptgs2* gene expression (tpm) in mouse tumor cells of subcutaneously implanted T cell–low and T cell–high tumors ($n$ = 8/group). (**E**) *PTGS2* expression in human PDA samples in the upper and lower deciles of cytolytic index ($n$ = 14/group). PDA samples retrieved from the TCGA data portal. (**F**) Survival of patients in the upper and lower deciles of *PTGS2* expression ($n$ = 17/group, TCGA PDA data set). (**G**) HOMER analysis of promoter regions of differentially expressed genes. Prediction of transcriptional regulators enriched in *Epha2*-WT and *Epha2*-KO tumor cells ($n$ = 3–8/group). (**H**) TGF-β signaling GSEA in *Epha2*-WT versus *Epha2*-KO tumor cells ($n$ = 3–8/group). (**I**) Relative expression of *Ptgs2* mRNA in PDA tumor cell clones treated with either PBS or TGF-β for 72 hours. Data from $n$ = 5 independent experiments. Color key represents the normalized Z score. (**J**) Relative expression of *Ptgs2* mRNA in control (ctrl, empty vector transduced) and *Smad3*- and *Smad4*-KO 6419c5 PDA tumor cell lines. Data from $n$ = 4 independent experiments. EV, empty vector. (**K** and **L**) Flow cytometric analysis of immune cell populations in control and *Smad3*-KO and *Smad4*-KO tumors ($n$ = 8–10/group). (**D**, **J**–**L**) Data are presented as boxplots, with horizontal lines and error bars indicating mean and range, respectively. (**E**) Data are presented as mean with error bars indicating SEM. Statistical differences determined by Students' $t$ test (**D** and **E**) or 1-way ANOVA with Tukey's HSD post test (**J**–**L**). The log-rank $P$ value was calculated using GraphPad Prism (**F**). *$P$ < 0.05; **$P$ < 0.01; ***$P$ < 0.001; ****$P$ < 0.0001.

5C). Tumor onset, defined by the age at ultrasonographic diagnosis, was significantly delayed in the KPCY$^{Ptgs2}$ mice, with median tumor-free survival of 140 days compared with 113 days in KPCY mice. Overall survival was significantly longer in KPCY$^{Ptgs2}$ mice compared with KPCY mice, with a log-rank hazard ratio of 0.5001 (95% CI of ratio 0.2941–0.8506).

*Genetic ablation of Ptgs2 suppresses tumor growth in a T cell–dependent manner*. To further study the role of *Ptgs2* in PDA and its association with *Epha2*, we used shRNA to knock down *Ptgs2* expression in a KPCY cell line. $PGE_2$ is the major prostanoid produced by PTGS2 enzymatic activity in KPCY cells (Figure 5D). As expected, *Ptgs2*-knockdown (*Ptgs2*-KD) resulted in a significant decrease in *Ptgs2* mRNA expression (Figure 5E) and $PGE_2$ production (Figure 5E). We then implanted control and *Ptgs2*-KD cells into immunocompetent mice, with or without CD4$^+$ and CD8$^+$ T cell depletion (Supplemental Figure 4A). While all mice injected with the control cell line developed tumors, 30%–50% of mice injected with *Ptgs2*-KD cells remained tumor free (Figure 5F), and those *Ptgs2*-KD tumors that did form were significantly smaller than control tumors (Figure 5F). T cell depletion abolished the survival benefit and suppressed tumor growth afforded by *Ptgs2* KD (Figure 5F). In addition, tumor growth was impeded following treatment with the selective PTGS2 inhibitor celecoxib (X) (Figure 5G), although unlike *Ptgs2* KD, the treatment did not result in a statistically significant survival benefit (Figure 5G).

To extend these results, we used CRISPR-Cas9 to knock out *Ptgs2* in a KPC cell line (*Ptgs2*-KO; Supplemental Figure 4, B and C). Despite exhibiting normal growth in vitro (Supplemental Figure 4, D and E), *Ptgs2*-KO cells were significantly impaired in tumor growth in vivo (Figure 5H). Specifically, 60%–70% of mice implanted with *Ptgs2*-KO cells failed to develop tumors (Figure 5H). Moreover, the *Ptgs2*-KO tumors that developed were significantly smaller than the tumors arising from control cells (Figure 5H). Consistent with our results using shRNA to knock down *Ptgs2*, the depletion of both CD4$^+$ and CD8$^+$ cells (Figure 5H) or either cell subset alone (not shown) was sufficient to abolish the control of tumor growth and overall survival benefit of *Ptgs2* ablation in *Ptgs2*-KO tumor-bearing mice. These results suggest that tumor cell–intrinsic expression of PTGS2 regulates T cell immune surveillance of mouse PDA tumors.

To determine whether *Ptgs2* also plays a non–cell-autonomous role in the tumor immune microenvironment, we used mice with a global deletion of *Ptgs2* as recipients for *Ptgs2*-KO and control cells. As before, implanted *Ptgs2*-KO PDA cells grew more slowly than control PDA cells following implantation, resulting in a significant survival advantage (Supplemental Figure 4F). However, systemic absence of *Ptgs2* had no additional protective effect for either overall survival or tumor growth (Supplemental Figure 4F), and WT tumors implanted in global *Ptgs2*-KO mice grew the same and were as lethal as when implanted into WT hosts. Thus, the antitumor effects of *Ptgs2* deletion result mainly from the tumor cell–intrinsic activity of PTGS2.

*Ablation of tumor cell–intrinsic Ptgs2 induces local immunity*. To investigate the effect of *Ptgs2* deletion on tumor cells and the tumor immune microenvironment, we analyzed *Ptgs2*-KO and control tumor cells in vitro by flow cytometry. Interestingly, *Ptgs2*-KO tumor cells had lower expression levels of EPHA2 protein on the cell surface compared with the control tumors (Supplemental Figure 5A). At the same time, *Ptgs2*-KO tumor cells expressed higher levels of MHC class I protein, yet lower levels of the immunosuppressive molecule PD-L1 (Supplemental Figure 5B). In addition, the proportion of immunosuppressive CD73$^+$ cells was dramatically lower among the *Ptgs2*-KO tumor cells (Supplemental Figure 5C). After subcutaneous growth for 12 to 13 days, *Ptgs2*-KO tumors weighed significantly less compared with the controls (Figure 6A). Accordingly, CD45$^-$CD31$^-$ tumor cells exhibited increased evidence of apoptosis (Figure 6B) as well as increased expression of MHC class I in *Ptgs2*-KO tumors compared with control tumors (Figure 6C). Although the proportion of PD-L1$^+$ tumor cells was higher in *Ptgs2*-KO tumors compared with control tumors, the proportion of tumor cells expressing the immunosuppressive molecules CD73 and CD39 was significantly lower in *Ptgs2*-KO tumors compared with the controls (Figure 6C).

As expected, *Ptgs2*-KO tumors were more T cell inflamed, with increased proportions of CD3$^+$ and CD8$^+$ T cells and a concomitant reduction in regulatory T cells (Figure 6D). We observed increased CD3$^+$ cell infiltration in the absence of tumor cell PTGS2 in mice bearing autochthonous tumors (Supplemental Figure 5D). Although total numbers of macrophages and dendritic cells were not different between control and *Ptgs2*-KO tumors, the expression of immune activation markers was significantly higher on type 1 classical dendritic cells (cDC1s) in *Ptgs2*-KO tumors (Figure 6E). Taken together, these results suggest that the deletion of *Ptgs2*, similarly to *Epha2* ablation, creates a more favorable TME for antitumor immunity and that the highly overlapping phenotypes of *Epha2* and *Ptgs2* deletion suggest a unified regulatory mechanism.

*Tumor cell–intrinsic Ptgs2 promotes a T cell–low TME in PDA*. To further explore the effect of tumor cell–intrinsic PTGS2 on the TME in PDA, we performed gain-of-function experiments by overexpressing *Ptgs2* in T cell–high tumor cell lines (*Ptgs2*-OE, Figure 7A). *Ptgs2* overexpression resulted in decreased infiltration by CD3$^+$ T cells in the TME (Figure 7, B–D). The proportions of CD4$^+$ and CD8$^+$ T cells as well as the percentages of activated CD8$^+$ T cells were significantly lower in *Ptgs2*-OE tumors (Figure 7D). Moreover, *Ptgs2* overexpression increased the proportions of infiltrating myeloid cells, especially gMDSCs, with a concomitant decrease in dendritic cell populations (Figure 7, E and F). To further assess whether tumor cell–intrinsic PTGS2 suppresses the response of PDA tumors to immunotherapy, we treated parental T cell–high tumors and *Ptgs2*-OE T cell–high tumors with the combination chemoimmunotherapy. Overexpression of *Ptgs2* completely abolished the response to therapy in both T cell–high cell lines, resulting in loss of tumor growth control and decreased survival in the *Ptgs2*-OE tumors (Figure 7G and Supplemental Figure 6). Together, these results support the conclusion that tumor cell–intrinsic PTGS2 promotes a T cell–low TME in PDA and consequently confers resistance to immunotherapy.

*Pharmacological inhibition of PTGS2 reverses PDA resistance to immunotherapy*. Finally, we sought to determine whether the pharmacological inhibition of PTGS2, alone or in combination with immunotherapy, would affect the growth of established tumors. PTGS2-sufficient tumor-bearing mice (day 18 after implantation) were randomly assigned to the following treatment arms: (a) i.p.

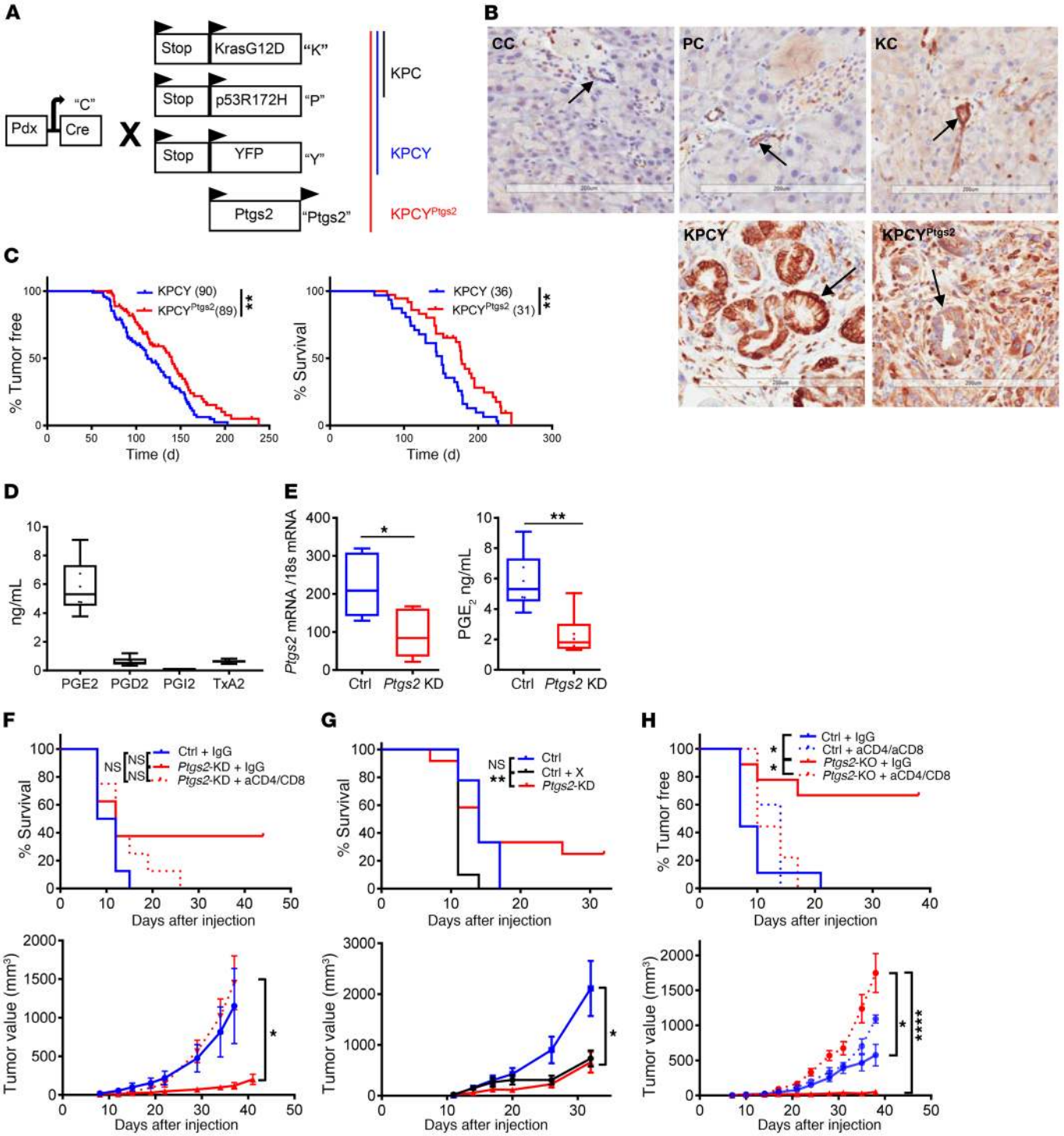


**Figure 5. *Ptgs2* deletion suppresses PDA growth.** (**A**) Graphic representation of pancreatic epithelial cell *Ptgs2*-deficient KPCY mouse. (**B**) PTGS2 protein staining (brown) in pancreatic ductal epithelial cells (arrows) of non–tumor-bearing mice (3–4 mice/group). Original magnification, ×20. (**C**) Kaplan-Meier curves of tumor-free (left) and overall survival (right) of KPCY and KPCY$^{Ptgs2}$ mice. Number of mice per group indicated in parentheses. (**D**) Extracellular prostanoid levels measured in control (nontarget shRNA transduced) cell lines cultured for 72 hours ($n$ = 6/group). (**E**) Relative expression of *Ptgs2* mRNA (left) and $PGE_2$ levels (right) in control (same as in **D**) and *Ptgs2*-KD (*Ptgs2* shRNA) KPCY cell lines after 72 hours in culture ($n$ = 6/group). (**F**) Control and *Ptgs2*-KD KPCY cell lines injected in syng8eneic CY mice receiving either isotype control (IgG) or anti-CD4– and anti-CD8–depleting antibodies (aCD4/aCD8; $n$ = 8-9/group); tumor-free survival (left) and tumor growth (right). (**G**) Control and *Ptgs2*-KD KPCY cell lines injected in syngeneic CY mice on regular chow (control) or 100 mg/kg celecoxib diet starting day 0 (ctrl + X; $n$ = 9–12/group); tumor-free survival (left) and tumor growth (right). (**H**) Control (Cas9 only transduced) and *Ptgs2*-KO (Cas9/ *Ptges2* gRNA transduced) KPC cell lines injected in WT mice receiving either isotype control (IgG) or anti-CD4– and anti-CD8– depleting (aCD4/aCD8) antibodies ($n$ = 5-9/group); tumor-free survival (left) and tumor growth (right). (**D** and **E**) Data are presented as boxplots, with horizontal lines and error bars indicating mean and range, respectively. Statistical significance measured by Student's unpaired $t$ test (**E**). The log-rank $P$ values for **C** were calculated in GraphPad Prism. Statistical analyses of tumor growth and survival for (**F**–**H**) performed using linear mixed-effects model with Tukey's HSD post test using the lme4 and the survival package in R. *$P < 0.05$; **$P < 0.01$; ****$P < 0.0001$.

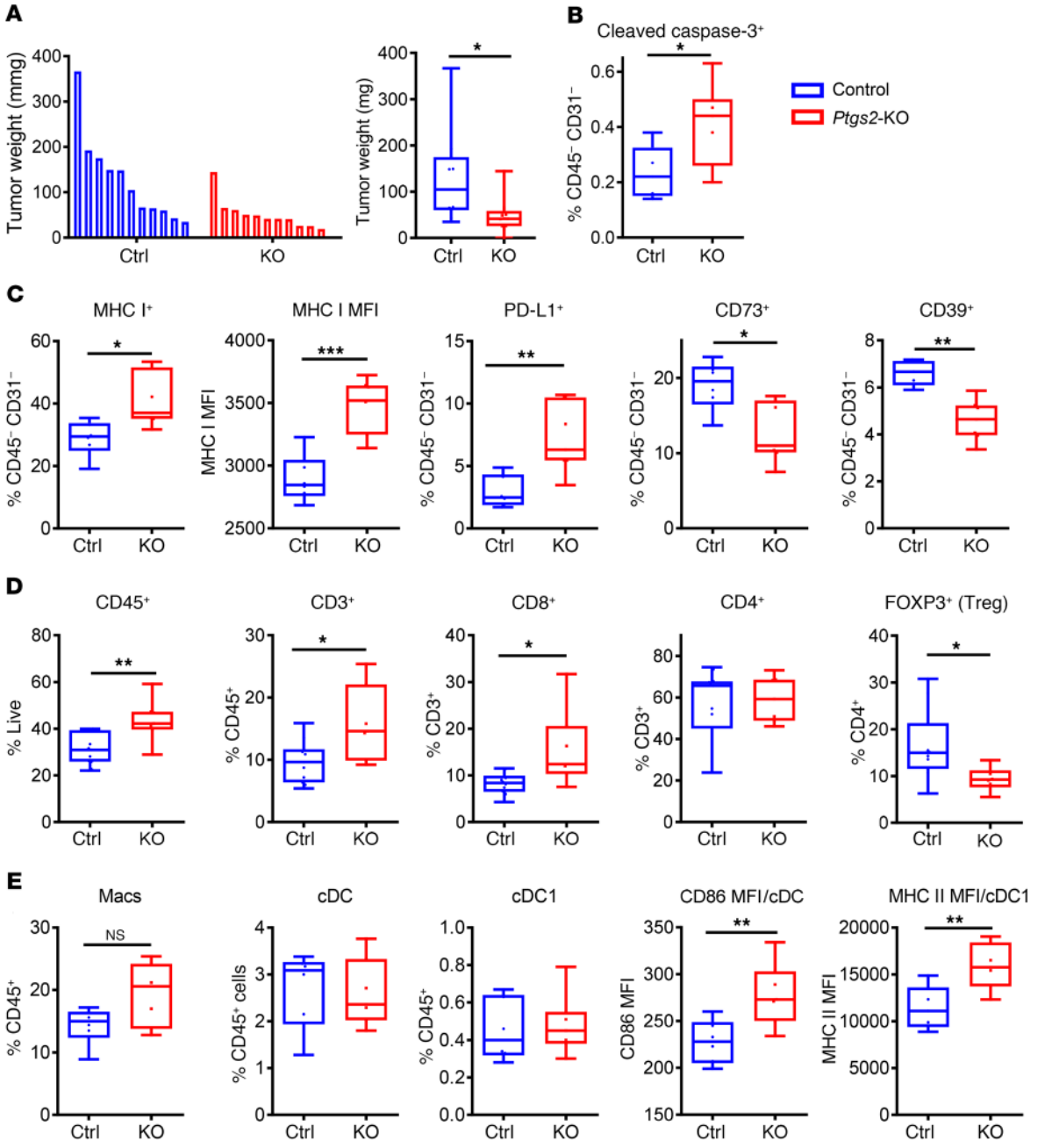


**Figure 6. *Ptgs2* ablation in PDA tumor cells increases tumor antigenicity and decreases immunosuppressive potential of the tumor.** (**A**) Individual (left) and average (right) weights of subcutaneously implanted control and *Ptgs2*-KO tumors 12 days after subcutaneous implantation. (**B**–**E**) Flow cytometric analysis of control and *Ptgs2*-KO tumors 12 to 13 days after subcutaneous implantation in WT mice. Representative experiments of 3 presented ($n$ = 6–12/group). Gating strategies presented in Supplemental Table 5. Data presented as box plots, with horizontal lines and error bars indicating mean and range, respectively. Statistical analysis between 2 groups performed using Student's unpaired $t$ test in GraphPad Prism. *$P < 0.05$; **$P < 0.01$; ***$P < 0.001$.

injection of an isotype control antibody (IgG); (b) celecoxib alone (X), (c) i.p. injections of anti–PD-1 antibody (P), (d) i.p. injections of agonistic CD40 antibody (F), and (e) combination celecoxib$^+$ anti–PD-1$^+$ agonistic CD40 (XPF). Monotherapies proved to be mostly ineffective, with only CD40 agonist reversing the tumor growth in 2 out of 9 mice (Figure 8A). Remarkably, combining PTGS2 inhibition with immunotherapy caused implanted tumor regression in 50% of cases or significantly inhibited the tumor growth (Figure 8, A and B). Most importantly, the combination therapy significantly increased the survival of autochthonous tumor-bearing KPCY mice compared with the untreated mice (Figure 8C). These results demonstrate that pharmacological inhibition of PTGS2 sensitizes PDA to immunotherapy.

## Discussion

Although the extent of passenger mutations in human cancers is a well-recognized determinant of response to checkpoint blockade immunotherapy, there is an increasing appreciation that heteroge-

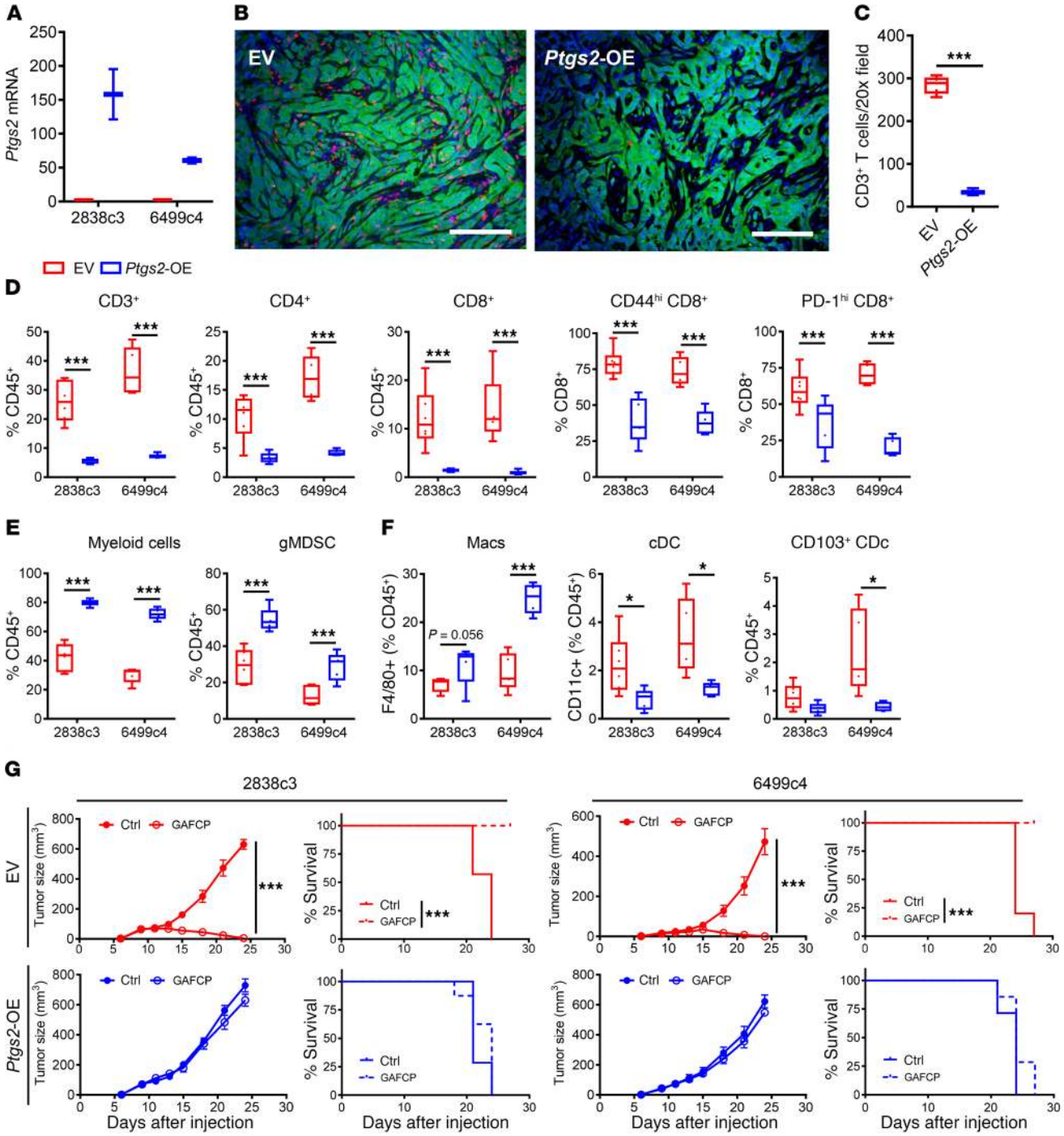


**Figure 7. Tumor cell–intrinsic *Ptgs2* promotes T cell–low TME and resistance to immunotherapy in PDA.** (**A**) Relative expression of *Ptgs2* mRNA measured by qPCR in T cell–high PDA tumor cell clones transduced with either empty vector (EV) or pCDH-FHC vector carrying mouse *Ptgs2* gene for overexpression (*Ptgs2*-OE). Representative data from $n = 3$ independent experiments. (**B** and **C**) Representative immunofluorescent staining images (**B**) and quantification (**C**) of $CD3^+$ T cells in 2838c3-EV and 2838c3-*Ptgs2*-OE subcutaneous tumors ($n = 5$/group): CD3 (red), YFP (green), and DAPI (blue). Original magnification, ×20. (**D**–**F**) Flow cytometric analysis of subcutaneously implanted empty vector or *Ptgs2*-OE tumors from indicated clones ($n = 5$-7/group). (**G**) Parental and *Ptgs2*-OE T cell–high tumor growth and mouse survival with or without GAFCP treatment. Tumor cells implanted subcutaneously into C57BL/6 mice ($n = 5$–8/group). GAFCP treatment started 9 days after implantation at 3–5 mm tumor diameter. (**A**, **C**–**F**) Data are presented as boxplots, with horizontal lines and error bars indicating mean and range, respectively. Statistical analysis between 2 groups calculated using Student's unpaired *t* test (**C**–**F**). The log-rank *P* values for Kaplan-Meier curves in **G** were calculated using GraphPad Prism. Statistical analysis of tumor growth curves performed using linear mixed-effects model with Tukey's HSD post test using lme4 and the survival package in R (**G**). $^*P < 0.05$; $^{***}P < 0.001$.

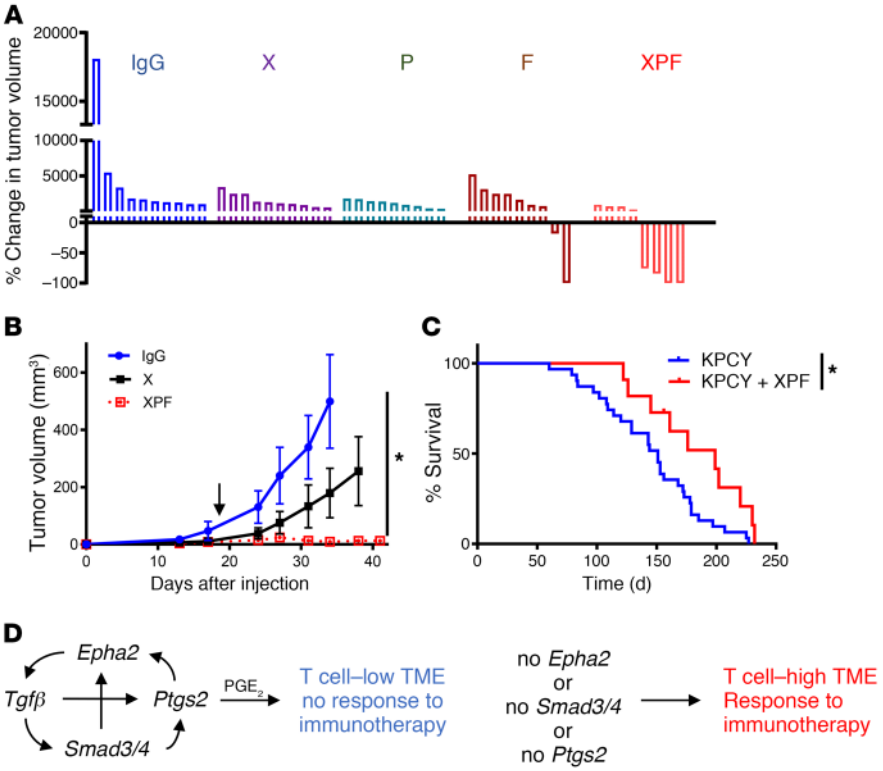


**Figure 8. Pharmacological inhibition of PTGS2 sensitizes PDA to immunotherapy.** (**A**) Changes in tumor volume 27 days after treatment start, relative to the baseline. KPC tumor cells were implanted subcutaneously in WT mice. IgG, X, P, F, and XPF treatments started 18 days after tumor implantation. Each column represents a single mouse ($n$ = 8–10/group). (**B**) Growth curves of subcutaneously implanted KPC tumors in WT mice ($n$ = 10/group). IgG, X, or XPF treatments started 18 days after implantation (black arrow). (**C**) Overall survival of KPCY mice without treatment and with XPF treatment started in mice with tumor volume of less than 20 mm$^3$ ($n$ = 11–36/group). (**D**) Schematic representation of EPHA2/TGF-β/SMAD/PTGS2 axis in PDA TME. Statistical analysis of tumor growth curves performed using linear mixed-effects model with Tukey's HSD post test using the lme4 (**B**). The log-rank $P$ values for Kaplan-Meier curves in **C** were calculated in GraphPad Prism. *$P$ < 0.05.

neous cancer cell–intrinsic properties apart from neoepitopes fundamentally regulate host immune response and the extent of tumor T cell infiltration (8, 17, 18, 20, 22, 32, 33). Across TCGA, the correlation between tumor mutational burden and a T cell–inflamed gene expression profile is poor (9, 13). Here, we identify EPHA2 and PTGS2 as tumor cell–intrinsic factors that regulate immune infiltration in the TME and modulate response to immunotherapy.

EPH receptor tyrosine kinases were first identified for their role in development, but several family members — including EPHA2 — also play a prominent role in malignancy. EPHA2 has been reported to promote tumor cell growth, migration, and metastasis as well as drug resistance in multiple types of malignancies (34–40). In PDA, increased *EPHA2* expression has been associated with poor clinical outcomes (41–45).

We observed that expression of *EPHA2* inversely correlates with the abundance of CD8$^+$ T cells in human and murine PDA tumors. Although we had previously identified CXCL1 as a determinant of CD8$^+$ cell exclusion in PDA (8), we observed no correlation between *EPHA2* and *CXCL1* expression levels in the human PDA TCGA data set ($n$ = 179, Pearson's $r$ = –0.04, $P$ = 0.618). In addition, *Cxcl1* was not differentially expressed in the mouse *Epha2*-WT and *Epha2*-KO tumor cell RNA-Seq data set ($n$ = 3-8/group, $P$ = 0.302). We functionally validated the role of EPHA2 in controlling immune infiltration and response to immunotherapy, changing our understanding of EPHA2 as an oncogene and an alternative determinant of tumor immunosuppression. Interestingly, *EPHA2* overexpression has been associated with resistance to MAPK inhibition in melanoma, in which resistance was accompanied by a decrease of tumor-infiltrating CD8$^+$ T cells (46). Similarly, molecular signatures of MAPK inhibitor–resistant tumors are shared across melanoma patients resistant to ICB (47). *Epha2* deletion results in the suppression of tumor cell–intrinsic SMAD signaling, suggesting a role for SMADs in modulating the immune infiltrate in PDA tumors. While we did not observe differential expression of TGF-β between *Epha2*-WT and *Epha2*-KO, it is possible that tumor cells utilize stromal TGF-β to upregulate SMAD signaling. This notion is supported by recent studies demonstrating that TGF-β signaling in cancer-associated fibroblasts (CAFs) prevents intratumoral T cell infiltration and suppresses the response to ICB (48, 49). However, in PDA, TGF-β is also shown to suppress IL-1–induced JAK/STAT signaling and tumor-promoting inflammatory CAF phenotype (50). Moreover, defective TGF-β signaling in mice is associated with accelerated progression of squamous cell carcinoma (51), indicating tissue- and cell context–dependent effects of TGF-β signaling. The results presented here deepen our understanding of the role of TGF-β and SMAD signaling in tumor immunity and suggest, as illustrated in Supplemental Figure 6B, that tumor cell–intrinsic determinants of the immune TME may act by establishing complex patterns of crosstalk between tumor cells and the surrounding stroma.

We have demonstrated that deletion of *Epha2*, *Smad3*, or *Smad4* decreased the expression of *Ptgs2*, the gene that encodes the COX-2 enzyme, resulting in reduced levels of proinflammatory $PGE_2$. While the *PTGS2* promoter region does not have the SMAD-binding motif (52), its transcriptional activators ETS and AP1 are enriched with SMAD3-binding sites (53, 54). Both COX-2 and $PGE_2$ have been implicated in tumor progression (55), mainly as mediators of angiogenesis and tumor cell proliferation and survival (56, 57). Importantly, elevated PTGS2 levels have been linked to unfavorable disease-free survival, larger tumor size, and higher metastatic incidence in breast, gastrointestinal, and colorectal cancers (58–62). It has been shown that in viral infections, $PGE_2$,

acting through EP2 and EP4 receptors, can impair cytotoxic T cell function and survival (63). We have previously shown that targeting either tumor-intrinsic or myeloid cell *Ptgs2* modulates immune infiltration and relieves immunosuppression, resulting in tumor growth inhibition, in a mouse model of breast cancer (64–67) As shown by others, genetic ablation of $PGE_2$-producing enzymes suppresses the growth of melanoma cells in mice by increasing the presence of cDC1s in the TME (68, 69). These studies support our finding that PTGS2 plays a critical role in antitumor immune suppression.

PTGS2 expression is highly upregulated in human PDA (61) and mutant $Kras^{G12D}$–driven mouse models of PDA (70–72). Aberrant PTGS2 expression in pancreas is associated with enhanced *Kras* expression and accelerated PanIN formation (73) as well as increased macrophage presence in PDA (70). Consequently, absence of *Ptgs2* delays PDA development in $Pdx1^{+}$; $Kras^{G12D/+}$; $Pten^{fl/+}$ mice, and the overexpression of *Ptgs2* promotes early onset and progression of PDA (72). The tumor-promoting effects of PTGS2 have been attributed to its ability to induce signaling pathways downstream of RAS (73), PI3K/AKT (72), and ERK (70). Here, we demonstrate that a modest decrease in *Ptgs2* expression translates into a substantial suppression of PGE2 production and, as a result, higher immune cell infiltrate and cytolytic activity in PDA. Our study suggests that the immunosuppressive functions of PTGS2 may have contributed to the tumor immune evasion and poor survival.

In summary, this study identifies an EPHA2/TGF-β/SMAD/PTGS2 signaling axis as a pathway deployed by PDA tumor cells to establish T cell–low TME (Figure 8D). Apart from its oncogenic potential, activation of this axis also frustrates response to immune therapy. Consequently, ablation of EPHA2 or PTGS2 reverses T cell exclusion and sensitizes tumors to immune therapy, even in the absence of strong neoepitopes. These findings not only predict which patients with pancreatic cancer might respond to novel immunotherapy combinations — such as a phase II study of chemotherapy, CD40, and PD1 agents currently underway (ClinicalTrials.gov NCT03214250) — but also suggest a potential role for selective inhibitors of PTGS2, TGF-β, or EPHA2 as additional components of future combination therapies.

## Methods

*Animals*. All WT C57BL/6 mice were purchased from The Jackson Laboratory and/or bred at the University of Pennsylvania. Kras-LSL-G12D/$^{+}$; Trp53-LSL-R172H/$^{+}$, Pdx1-Cre, and Rosa-LSL-YFP (KPCY) mice (74, 75) were bred in-house, backcrossed for over 10 generations with C57BL/6J mice (Jackson Laboratories), and assessed at the DartMouse Speed Congenic Core facility at the Geisel School of Medicine at Dartmouth College (Hanover, New Hampshire, USA). KPCY mice were then crossed with C57BL/6 mice with LoxP sites (flox/flox) inserted in introns 5 and 8 of the *Ptgs2* gene (76) to generate $KPCY^{Ptgs2}$ mice. Seven-to eight-week-old tamoxifen-inducible $Cre^{+/-}$-$Ptgs2^{fl/fl}$ mice (77) provided in house were treated with 100 mg tamoxifen (Sigma-Aldrich) for 5 days to generate *Ptgs2* global KO mice (gKO). For the survival studies, young (less than 10 weeks old), KPCY and $KPCY^{Ptgs2}$ mice were monitored for the development of pancreatic tumors by abdominal palpation. After 10 weeks, all mice were monitored by ultrasound imaging (Vevo 2100 Imaging System with 55MHz MicorScan transducer, Visula Sonics) once a week until tumor discovery, after which the tumor growth was monitored by biweekly ultrasound imaging. For tumor-bearing mice, end point criteria included tumor volume exceeding 500 $mm^3$, severe cachexia, or weakness and inactivity.

*Tumor cells*. KPCY and KPC cell lines were derived from single-cell suspensions of PDA tissues as previously described (78) and tested by the Research Animal Diagnostic Laboratory (RADIL) at the University of Missouri (Columbia, Missouri, USA), according to the Infectious Microbe PCR Amplification Test (IMPACT) II profile. All mouse pancreatic tumor cell clones were isolated from late-stage primary tumors from KPCY mice on a C57BL/6 background and generated by limiting dilution (Supplemental Table 1). Cells were cultured in DMEM (high glucose without sodium pyruvate) with 10% FBS (Gibco; Thermo Fisher Scientific) and glutamine (2 mM). The clones were regularly tested using the MycoAlert Mycoplasma Detection Kit (Lonza).

*Analysis of TCGA and ICGC data sets*. Data showing the expression levels of *CD8A* and *EPHA2* genes in human PDA tumors were from TCGA. The gene expression profiles of these samples were downloaded and processed for transcripts per million (tpm), as previously described (79). Pearson's correlation analysis was used to determine $R^2$ values and *P* values. All correlation analysis resulted in *P* values of less than 0.0001, identified as significant. Patient survival and normalized RSEM counts (rsem.genes.normalized_results) for tumor *PTGS2* and *EPHA2* were retrieved from the RNA-Seq analysis of PDAC patients in the TCGA database, using the OncoLnc tool (80). The log-rank *P* values were calculated for the upper and lower deciles ($n$ = 17/group) of *PTGS2* and *EPHA2* expression (TCGA data as of July 2018), using GraphPad Prism7. Differential *PTGS2* expression in cytolytic low and high tumors was analyzed with RNA-Seq data for PDA samples retrieved from the TCGA data set. Length-scaled tpm counts were determined using output from kallisto version 0.43.0 with default parameters. The reference transcriptome was retrieved from Ensembl in December 2017 (release 90). Cytolytic index was calculated for all samples, as previously described (14). Samples with a cytolytic index equal to or more extreme than the top and bottom deciles were used in the differential gene expression analysis. Gene-level differential expression for *PTGS2* was determined using the DESeq2 package with default parameters and the Benjamini-Hochberg correction (81). Metascape analysis was done, using default parameters (http://metascape.org/gp/index.html#/main/step1). Output results from the online Metascape analysis were graphed using GraphPad Prism.

*Analysis of RNA-Seq, differential gene expression, and GSEA molecular signature analysis*. RNA samples were extracted from sorted $YFP^{+}$ tumor cells from subcutaneously implanted tumors using the QIAGEN RNeasy Micro Kit following the manufacturer's instructions. RNA was sent out to a commercial company (Novogene) for library preparation and high-throughput sequencing using Illumina sequencers to generate paired end 150 bp data. Fastq files were checked for quality using FastQC. Raw counts of gene transcripts were obtained using the alignment-independent tool Salmon, using standard settings (82). The raw count matrix was subsequently imported into R-studio (R version 3.3.3) and used as input for DESeq2 following the vignette of the package for normalization and differential gene expression analysis (81). Salmon was also used to normalize and quantitate gene expression in tpm through quasialignment. Differentially expressed genes from DESeq2 analysis were used as input for MSigDB GSEA (83).

*Lentiviral transduction of tumor cells for CRISPR-mediated ablation*. The CRISPR vector, lentiCRISPR v2, was a gift from Feng Zhang (Massachusetts Institute of Technology, Cambridge, Massachusetts, USA) (Addgene plasmid 52961) (84). The vector and pVSVg and psPAX2 lentiviral packaging plasmids (Addgene) were cotransfected into 293T cells using PEI reagent. Lentiviral particles were collected 48 hours after transfection and filtered for usage. KPC cells transduced either with Cas9-Puro (control) or Cas9-guide-Puro (KO) were selected with 2 μg/ml puromycin. Single cells were picked from the KO cell line and expanded into clones. Deletion efficiencies were assessed by gene-specific quantitative PCR (qPCR) analysis. CRISPR sequences utilized were as follows: *Epha2,* ACAACGTGGTATCCGGCGACC; *Epha2*, BTTCGCTGTCGAAGCACGCAA; *Ptgs2*, ATTCAAGACAGATCATAAGCG; *Ptgs2*, BCCATAGTGCACATTGTAAGT; *Smad3*, AGCTCCATGGCCCGTAATTCA; *Smad3*, BACCTACCTGGAATATTGCTC; *Smad4*, AGCCAAGTAATCGCGCATCAA; and *Smad4*, BTCCGTTGATGCGCGATTACT.

*Lentiviral transduction of tumor cells for shRNA-mediated KD*. KPCY cells were transduced with Mission plKO.1-puro Transduction Lentiviral Particles (Sigma-Aldrich) carrying either nontarget control shRNA or *Ptgs2* shRNA (KD) and selected with 2 μg/ml puromycin (Sigma-Aldrich).

*Lentiviral transduction of tumor cells for overexpression of target genes*. The pCDH-EF1-FHC vector was a gift from Richard Wood (MD Anderson Cancer Center, Houston, Texas, USA) (Addgene plasmid 64874) (85). The *Ptgs2* gene was cloned into the vector for constitutive overexpression. The vector and pVSVg and psPAX2 lentiviral packaging plasmids (Addgene) were cotransfected into 293T cells using PEI reagent. Lentiviral particles were collected 48 hours after transfection and filtered for usage. Tumor cells were transduced and selected with 2 μg/ml puromycin. Overexpression efficiencies were assessed by gene-specific qPCR analysis.

*qPCR analysis for gene expression*. RNA was prepared from cultured tumor cells or sorted cells from implanted tumors using the RNeasy Mini Kit or the RNeasy Micro Kit (QIAGEN). cDNA was generated using the High-Capacity cDNA Reverse Transcription Kit (Life Technologies). qPCR analysis was performed using SsoAdvanced SYBR reagent (Bio-Rad) and Bio-Rad qPCR Platform, and results were normalized to the expression of Tbp. Primer sequences utilized for qPCR were as follows: *Epha2*, forward-GCACAGGGAAAGGAAGTTGTT; *Epha2*, reverse-CATGTAGATAGGCATGTCGTCC; *Ptgs2*, forward-CATGTAGATAGGCATGTCGTCC; *Ptgs2*, reverse-AGAAGCGTTTGCGGTACTCAT; *Smad3*, forward-CACGCAGAACGTGAACACC; *Smad3*, reverse-GGCAGTAGATAACGTGAGGGA; *Smad4*, forward-ACACCAACAAGTAACGATGCC; and *Smad4*, reverse-GCAAAGGTTTCACTTTCCCCA.

For PCR reactions in Figure 4 and Supplemental Figure 4, total RNA from tumor cell lines was isolated (RNeasy, QIAGEN) and reverse transcribed (Reverse Transcription Kit, Applied Biosystems) according to the manufacturer's instructions. Real-time qPCR for *Ptgs2* and *18s* mRNA was performed using inventoried gene expression assays and TaqMan Universal PCR Master Mix (Applied Biosystems). PCR products were detected using the Vii A7 Real-Time PCR System (Applied Biosystems). Results were analyzed using the comparative Ct method and normalized to 18s RNA.

*PGE2 measurements*. Prostaglandins and their metabolites were measured by ultra-high-pressure liquid chromatography/tandem mass spectrometry (UHPLC/MS/MS), using negative electrospray ionization and selected reaction monitoring (SRM) techniques on a Quantum Ultra interfaced to an Accela UHPLC system (Thermo Scientific), as described previously (67).

*Implantation of tumor cells*. *Epha2*-WT and *Epha2*-KO cultured tumor cells were dissociated into single cells with 0.25% trypsin (Gibco, Thermo Fisher Scientific), washed with serum-free DMEM twice, and counted in preparation for subcutaneous or orthotopic implantations. $1.5 \times 10^5$ to $3.0 \times 10^5$ Tumor cells were implanted subcutaneously, and $3.0 \times 10^4$ to $5.0 \times 10^4$ tumor cells were implanted orthotopically into 6- to 8-week-old C57BL/6 mice. Tumors were harvested 3 to 4 weeks following implantation. Control and *Ptgs2*-KD were prepared as above. For tumor growth and survival studies, the cells were resuspended in sterile PBS, $1.0 \times 10^5$/100 μl, and injected subcutaneously in the flanks of T cell–replete or T cell–depleted CY male and female host mice. KPC control and *Ptgs2*-KO cells were prepared as above. For tumor growth and survival experiments, $1.0 \times 10^5$/100 μl cells in 100 μl sterile PBS were injected into the flanks of 6- to 8-week-old T cell–replete or T cell–depleted female C57BL/6 mice or into the flanks of male and female tamoxifen-induced global *Ptgs2*-KO (gKO) (77) hosts. For tumor flow cytometry, 4 to $5 \times 10^5$ cells/100 μL sterile PBS were injected into the flanks of 6- to 8-week-old female C57BL/6 mice. Tumor tissues were harvested and analyzed 12 to 13 days after implantation.

*Subcutaneous tumor growth and regression assessments*. For tumor growth kinetics, tumors were measured every 3 days. Tumor length and width were measured with calipers, and tumor volumes were then calculated as length × width$^2$/2. Tumor volumes of 500 mm$^3$ were used as an end point for survival analysis. Tumor regressions and waterfall plots were calculated using the initial tumor size at the start of treatment and tumor size 21 or 27 days later.

*Treatments and T cell depletions*. For experiments shown in Figure 2 and Supplemental Figure 2, gemcitabine (Hospira) and Nab-paclitaxel (Abraxane, Celgene) were purchased from the Hospital of the University of Pennsylvania Pharmacy. Gemcitabine was procured as pharmaceutical grade suspension at 38 mg/mL, diluted to 12 mg/mL in PBS, and administered at 120 mg/kg via i.p. injection. Abraxane was purchased as a pharmaceutical grade powder resuspended at 12 mg/mL in PBS for i.p. injection at a dose of 120 mg/kg. Vehicle control mice received the equivalent to a nab-paclitaxel dose of human albumin (huAlb; MilliporeSigma). Chemotherapy was injected at days 9 to 14, when tumor size was 3 to 5 mm. For anti-CD40 agonist treatment, mice were injected i.p. with 100 μg of either agonistic CD40 rat anti-mouse IgG2a mAb (clone FGK45, endotoxin-free) or the isotype control IgG2a mAb (clone 2A3, BioXcell), administered 48 hours after chemotherapy. For checkpoint blockade treatment, mice were injected i.p. with 200 μg of PD-1 (clone RMP 1-14, BioXcell) and 200 μg CTLA4 (clone 9H10, BioXcell), starting at days 9 to 14 (therapy start time point), using 7 and 3 doses, respectively. Control mice received the isotype control IgG2a mAb (clone 2A3, BioXcell) on treatment days. For the experiments in Figure 4, CD4$^+$ and CD8$^+$ T cells were depleted using i.p. injections of 200 mg endotoxin-free anti-CD4 (clone GK1.5, BioXcell) and anti-CD8 (clone 2.43, BioXcell) antibodies 3 days prior to tumor implantation and twice a week thereafter, for the duration of the experiment. Control groups received IgG2b isotype control antibody (BioXcell). T cell depletion in the peripheral blood was confirmed by flow cytometry. In treatment groups, starting at day 18, mice received either 100 mg/kg/d celecoxib in chow

(Envigo) or anti–PD-1 (BioXcell) i.p. on days 18, 21, 24, and 27, aCD40 (BioXcell) i.p. on day 21, or a combination of celecoxib diet with i.p. injections of anti–PD-1 and anti-CD40. Control groups in these experiments received rat IgG2a isotype control antibody (BioXcell). KPCY tumor-bearing mice with less than 40 $mm^3$ tumors by ultrasound measurement were placed on a 50 mg/kg celecoxib diet together with anti–PD-1 antibody injections every third day starting from the day of diagnosis (8 doses of anti–PD-1 in total). The same mice received a single dose of aCD40 with the second dose of anti–PD-1.

*Flow cytometry of implanted tumors*. For the flow cytometric analyses, tumors were digested in 1 mg/ml collagenase with protease inhibitor (Sigma-Aldrich) and filtered through a 70 μm cell strainer. Samples were stained for cell-surface molecules then fixed and permeabilized (eBioscience Intracelluar Fixation &Permeabilization Buffer Set, Invitrogen), further stained for intracellular targets, and analyzed by flow cytometry using the BD FACSCanto system (BD Biosciences) and Flow Jo software (Treestar). The antibodies used for cell-surface and intracellular stainings and the gating strategies are listed in Supplemental Tables 2, 3, 4, and 5.

*Immunofluorescent and immunohistochemistry stainings*. For CD3, PTGFRβ,and αSMA stainings, tissues were fixed in Zn-formalin for 24 hours and embedded in paraffin. Sections were deparaffinized, rehydrated, and prepared by antigen retrieval for 6 minutes each and then blocked in 5% donkey serum for 1 hour at room temperature, incubated with primary antibodies (Supplemental Table 6) overnight at 4°C, washed, incubated with secondary antibodies for 1 hour at room temperature, washed again, and mounted. Slides were visualized and imaged using an Olympus IX71 inverted multicolor fluorescent microscope and a DP71 camera. For CD3 quantification, stained cells were counted in 5 fields per sample. PTGFRβ and αSMA stainings were quantified with ImageJ software (NIH) using default settings. PTGS2 staining was performed on Zn-formalin–fixed, paraffin–embedded pancreata using anti-PTGS2 rabbit monoclonal antibody (Thermo Fisher Scientific). Slides were scanned with an Aperio CS-O scanner, and images were visualized using Aperio ImageScope software (Leica Biosystems).

*In vitro treatment with IFN-β and IFN-γ for MHC I expression analysis*. Cultured tumor cells were induced with 100 ng/mL of IFN-γ (Peprotech) and/or 1,000 units/mL IFN-β (PBL Assay Science) for 24 hours before analysis. Single cells were then stained with MHC I mAb (BioLegend) and analyzed by flow cytometry.

*Data resources*. The RNA-Seq data were deposited in the NCBI's Gene Expression Omnibus database (GSE120208).

*Software*. PRISM software and R were used for the data processing, statistical analysis, and result visualization (http://www.graphpad.com). The R language and environment for statistical computing and graphics (https://www.r-project.org) were utilized in this study for the statistical and bioinformatics analysis of RNA-Seq data. The R packages used for the analysis described in Methods were obtained from the Bioconductor (https://www.bioconductor.org) and CRAN (https://cran.r-project.org/web/packages/available_packages_by_name.html).

*Contacts for reagent and resource sharing*. Request for more information about this manuscript and reagents should be directed to the corresponding authors Ben Z. Stanger (bstanger@upenn.edu) and Robert H. Vonderheide (rhv@upenn.edu).

*Statistics*. Statistical comparisons between 2 groups were performed using Student's unpaired *t* test. For comparisons between multiple groups, 1-way ANOVA with Tukey's honestly significant difference (HSD) post test was used. For survival comparison between 2 groups, log-rank *P* values of Kaplan-Meier curves were determined with GraphPad Prism 7. Survival curve comparisons between multiple groups and tumor growth curve analyses were performed using linear mixed-effects modes with Tukey's HSD post test using the lme4 and the survival package in R. On graphs, error bars represent either range or SEM, as indicated in legends. $P < 0.05$ was considered statistically significant.

*Study approval*. All animal procedures were conducted following NIH guidelines. All mouse protocols were reviewed and approved by the Institutional Animal Care and Use committee (IACUC) of the University of Pennsylvania.

## Author contributions

RHV, BZS, NM, JL, and GAF conceived the project. RHV, BZS, NM, JL, and GAF developed the methods. JL, LPR, AJR, JHL, and YHS developed the software. NM and JL analyzed the data. NM, JL, LPR, AJR, JHL, YHS, FY, NG, TY, and YS performed experiments. NM, JL, LPR, AJR, YHS, FY, LQ, TY, YS, NG, JWT, and KTB curated data. NM, JL, BZS, and RHV wrote the manuscript.

## Acknowledgments

We thank members of the Vonderheide and Stanger laboratories for technical help and scientific discussions. This work was supported by grants from the NIH (R01-CA169123 and R01-CA229803 to BZS and RHV), the Parker Institute for Cancer Immunotherapy (to RHV and KTB), the Penn Center for Molecular Studies in Digestive and Liver Diseases (P30-DK050306), the ACC Support Grant (P30-CA016520), and the Blavatnik Family Foundation (to JL). Computational and bioinformatic analysis was performed on the Penn Medicine Academic Computing Services High-Performance Computing (Penn HPC) environment with support from NIH 1S10OD012312. GAF is the recipient of a merit award from the American Heart Association, and his work is also supported by the National Heart, Lung, and Blood Institute, the National Center for Advancing Translational Sciences, and the Volkswagen Foundation.

Address correspondence to: Robert H. Vonderheide, 12 South Pavilion, 3400 Civic Center Boulevard, Philadelphia, Pennsylvania 19104, USA. Phone: 215.662.3929; Email: rhv@upenn.edu. Or to: Ben Z. Stanger, 421 Curie Boulevard, 512 BRB II/III, Philadelphia, Pennsylvanaia 19104, USA. Phone: 215.746.5559; Email: bstanger@upenn.edu.

1. Peggs KS, Quezada SA. Ipilimumab: attenuation of an inhibitory immune checkpoint improves survival in metastatic melanoma. *Expert Rev Anticancer Ther*. 2010;10(11):1697–1701.
2. Larkin J, Hodi FS, Wolchok JD. Combined nivolumab and ipilimumab or monotherapy in untreated melanoma. *N Engl J Med*. 2015;373(13):1270–1271.
3. Le DT, et al. Mismatch repair deficiency predicts response of solid tumors to PD-1 blockade. *Science*. 2017;357(6349):409–413.
4. Topalian SL, et al. Safety, activity, and immune correlates of anti–PD-1 antibody in cancer. *N Engl J Med*. 2012;366(26):2443–2454.
5. Sanmamed MF, Chen L. A paradigm shift in

cancer immunotherapy: from enhancement to normalization. *Cell*. 2018;175(2):313–326.
6. Tumeh PC, et al. PD-1 blockade induces responses by inhibiting adaptive immune resistance. *Nature*. 2014;515(7528):568–571.
7. Spranger S. Mechanisms of tumor escape in the context of the T-cell-inflamed and the non-T-cell-inflamed tumor microenvironment. *Int Immunol*. 2016;28(8):383–391.
8. Li J, et al. Tumor cell–intrinsic factors underlie heterogeneity of immune cell infiltration and response to immunotherapy. *Immunity*. 2018;49(1):178–193.e7.
9. Cristescu R, et al. Pan-tumor genomic biomarkers for PD-1 checkpoint blockade-based immunotherapy. *Science*. 2018;362(6411):eaar3593.
10. Morrison AH, Byrne KT, Vonderheide RH. Immunotherapy and prevention of pancreatic cancer. *Trends Cancer*. 2018;4(6):418–428.
11. Bayne LJ, et al. Tumor-derived granulocyte-macrophage colony-stimulating factor regulates myeloid inflammation and T cell immunity in pancreatic cancer. *Cancer Cell*. 2012;21(6):822–835.
12. Jiang H, et al. Targeting focal adhesion kinase renders pancreatic cancers responsive to checkpoint immunotherapy. *Nat Med*. 2016;22(8):851–860.
13. Spranger S, et al. Density of immunogenic antigens does not explain the presence or absence of the T-cell-inflamed tumor microenvironment in melanoma. *Proc Natl Acad Sci U S A*. 2016;113(48):E7759–E7768.
14. Balli D, Rech AJ, Stanger BZ, Vonderheide RH. Immune cytolytic activity stratifies molecular subsets of human pancreatic cancer. *Clin Cancer Res*. 2017;23(12):3129–3138.
15. Chao T, Furth EE, Vonderheide RH. CXCR2-dependent accumulation of tumor-associated neutrophils regulates T-cell immunity in pancreatic ductal adenocarcinoma. *Cancer Immunol Res*. 2016;4(11):968–982.
16. Seifert L, et al. The necrosome promotes pancreatic oncogenesis via CXCL1 and Mincle-induced immune suppression. *Nature*. 2016;532(7598):245–249.
17. Spranger S, Bao R, Gajewski TF. Melanoma-intrinsic β-catenin signalling prevents anti-tumour immunity. *Nature*. 2015;523(7559):231–235.
18. Welte T, et al. Oncogenic mTOR signalling recruits myeloid-derived suppressor cells to promote tumour initiation. *Nat Cell Biol*. 2016;18(6):632–644.
19. Peng W, et al. Loss of PTEN promotes resistance to T cell-mediated immunotherapy. *Cancer Discov*. 2016;6(2):202–216.
20. Wang G, et al. Targeting YAP-dependent MDSC infiltration impairs tumor progression. *Cancer Discov*. 2016;6(1):80–95.
21. Kortlever RM, et al. Myc cooperates with Ras by programming inflammation and immune suppression. *Cell*. 2017;171(6):1301–1315.e14.
22. Jerby-Arnon L, et al. A cancer cell program promotes T cell exclusion and resistance to checkpoint blockade. *Cell*. 2018;175(4):984–997.e24.
23. Winograd R, et al. Induction of T-cell immunity overcomes complete resistance to PD-1 and CTLA-4 blockade and improves survival in pancreatic carcinoma. *Cancer Immunol Res*. 2015;3(4):399–411.
24. Byrne KT, Vonderheide RH. CD40 stimulation obviates innate sensors and drives T cell immunity in cancer. *Cell Rep*. 2016;15(12):2719–2732.
25. Tandon M, Vemula SV, Mittal SK. Emerging strategies for EphA2 receptor targeting for cancer therapeutics. *Expert Opin Ther Targets*. 2011;15(1):31–51.
26. Ino Y, et al. Immune cell infiltration as an indicator of the immune microenvironment of pancreatic cancer. *Br J Cancer*. 2013;108(4):914–923.
27. Hiraoka N, Ino Y, Yamazaki-Itoh R, Kanai Y, Kosuge T, Shimada K. Intratumoral tertiary lymphoid organ is a favourable prognosticator in patients with pancreatic cancer. *Br J Cancer*. 2015;112(11):1782–1790.
28. Balachandran VP, et al. Identification of unique neoantigen qualities in long-term survivors of pancreatic cancer. *Nature*. 2017;551(7681):512–516.
29. Bayne LJ, Vonderheide RH. A myeloid-derived suppressor cell-mediated T-cell suppression assay for functional evaluation of immune cells in tumor-bearing mice. *Cold Spring Harb Protoc*. 2013;2013(9):849–853.
30. Tian J, et al. Cyclooxygenase-2 regulates TGFβ-induced cancer stemness in triple-negative breast cancer. *Sci Rep*. 2017;7:40258.
31. Kumai T, et al. Tumor-derived TGF-β and prostaglandin E2 attenuate anti-tumor immune responses in head and neck squamous cell carcinoma treated with EGFR inhibitor. *J Transl Med*. 2014;12:265.
32. Wellenstein MD, de Visser KE. Cancer-cell-intrinsic mechanisms shaping the tumor immune landscape. *Immunity*. 2018;48(3):399–416.
33. Spranger S, Gajewski TF. Impact of oncogenic pathways on evasion of antitumour immune responses. *Nat Rev Cancer*. 2018;18(3):139–147.
34. Fang WB, Brantley-Sieders DM, Parker MA, Reith AD, Chen J. A kinase-dependent role for EphA2 receptor in promoting tumor growth and metastasis. *Oncogene*. 2005;24(53):7859–7868.
35. Brantley-Sieders DM, et al. The receptor tyrosine kinase EphA2 promotes mammary adenocarcinoma tumorigenesis and metastatic progression in mice by amplifying ErbB2 signaling. *J Clin Invest*. 2008;118(1):64–78.
36. Zhuang G, et al. Elevation of receptor tyrosine kinase EphA2 mediates resistance to trastuzumab therapy. *Cancer Res*. 2010;70(1):299–308.
37. Amato KR, et al. Genetic and pharmacologic inhibition of EPHA2 promotes apoptosis in NSCLC. *J Clin Invest*. 2014;124(5):2037–2049.
38. Song W, Ma Y, Wang J, Brantley-Sieders D, Chen J. JNK signaling mediates EPHA2-dependent tumor cell proliferation, motility, and cancer stem cell-like properties in non-small cell lung cancer. *Cancer Res*. 2014;74(9):2444–2454.
39. Amato KR, et al. Genetic and pharmacologic inhibition of EPHA2 promotes apoptosis in NSCLC. *J Clin Invest*. 2014;124(5):2037–2049.
40. Amato KR, et al. EPHA2 blockade overcomes acquired resistance to EGFR kinase inhibitors in lung cancer. *Cancer Res*. 2016;76(2):305–318.
41. Duxbury MS, Ito H, Zinner MJ, Ashley SW, Whang EE. EphA2: a determinant of malignant cellular behavior and a potential therapeutic target in pancreatic adenocarcinoma. *Oncogene*. 2004;23(7):1448–1456.
42. Mudali SV, Fu B, Lakkur SS, Luo M, Embuscado EE, Iacobuzio-Donahue CA. Patterns of EphA2 protein expression in primary and metastatic pancreatic carcinoma and correlation with genetic status. *Clin Exp Metastasis*. 2006;23(7-8):357–365.
43. Yachida S, Iacobuzio-Donahue CA. The pathology and genetics of metastatic pancreatic cancer. *Arch Pathol Lab Med*. 2009;133(3):413–422.
44. Van den Broeck A, Vankelecom H, Van Eijsden R, Govaere O, Topal B. Molecular markers associated with outcome and metastasis in human pancreatic cancer. *J Exp Clin Cancer Res*. 2012;31:68.
45. Koshikawa N, Minegishi T, Kiyokawa H, Seiki M. Specific detection of soluble EphA2 fragments in blood as a new biomarker for pancreatic cancer. *Cell Death Dis*. 2017;8(10):e3134.
46. Hugo W, et al. Non-genomic and immune evolution of melanoma acquiring MAPKi resistance. *Cell*. 2015;162(6):1271–1285.
47. Hugo W, et al. Genomic and transcriptomic features of response to anti–PD-1 therapy in metastatic melanoma. *Cell*. 2016;165(1):35–44.
48. Tauriello DVF, et al. TGFβ drives immune evasion in genetically reconstituted colon cancer metastasis. *Nature*. 2018;554(7693):538–543.
49. Mariathasan S, et al. TGFβ attenuates tumour response to PD-L1 blockade by contributing to exclusion of T cells. *Nature*. 2018;554(7693):544–548.
50. Biffi G, et al. IL1-induced JAK/STAT signaling is antagonized by TGFβ to shape CAF heterogeneity in pancreatic ductal adenocarcinoma. *Cancer Discov*. 2019;9(2):282–301.
51. White RA, Malkoski SP, Wang XJ. TGFβ signaling in head and neck squamous cell carcinoma. *Oncogene*. 2010;29(40):5437–5446.
52. Morikawa M, Koinuma D, Miyazono K, Heldin CH. Genome-wide mechanisms of Smad binding. *Oncogene*. 2013;32(13):1609–1615.
53. Koinuma D, et al. Chromatin immunoprecipitation on microarray analysis of Smad2/3 binding sites reveals roles of ETS1 and TFAP2A in transforming growth factor beta signaling. *Mol Cell Biol*. 2009;29(1):172–186.
54. Appleby SB, Ristimäki A, Neilson K, Narko K, Hla T. Structure of the human cyclo-oxygenase-2 gene. *Biochem J*. 1994;302(Pt 3):723–727.
55. Wang D, Dubois RN. Eicosanoids and cancer. *Nat Rev Cancer*. 2010;10(3):181–193.
56. Xu L, et al. COX-2 inhibition potentiates antiangiogenic cancer therapy and prevents metastasis in preclinical models. *Sci Transl Med*. 2014;6(242):242ra84.
57. Hu H, et al. Elevated COX-2 expression promotes angiogenesis through EGFR/p38-MAPK/Sp1-dependent signalling in pancreatic cancer. *Sci Rep*. 2017;7(1):470.
58. Ristimäki A, et al. Prognostic significance of elevated cyclooxygenase-2 expression in breast cancer. *Cancer Res*. 2002;62(3):632–635.
59. Xu F, et al. Clinicopathological and prognostic significance of COX-2 immunohistochemical expression in breast cancer: a meta-analysis. *Oncotarget*. 2017;8(4):6003–6012.
60. Bhandari P, et al. Prognostic significance of cyclooxygenase-2 (COX-2) expression in patients with surgically resectable adenocarcinoma of the oesophagus. *BMC Cancer*. 2006;6:134.
61. Yip-Schneider MT, et al. Cyclooxygenase-2

expression in human pancreatic adenocarcinomas. *Carcinogenesis*. 2000;21(2):139–146.
62. Wang D, Dubois RN. The role of COX-2 in intestinal inflammation and colorectal cancer. *Oncogene*. 2010;29(6):781–788.
63. Chen JH, et al. Prostaglandin E2 and programmed cell death 1 signaling coordinately impair CTL function and survival during chronic viral infection. *Nat Med*. 2015;21(4):327–334.
64. Chen EP, et al. Myeloid Cell COX-2 deletion reduces mammary tumor growth through enhanced cytotoxic T-lymphocyte function. *Carcinogenesis*. 2014;35(8):1788–1797.
65. Markosyan N, Chen EP, Smyth EM. Targeting COX-2 abrogates mammary tumorigenesis: Breaking cancer-associated suppression of immunosurveillance. *Oncoimmunology*. 2014;3:e29287.
66. Markosyan N, Chen EP, Evans RA, Ndong V, Vonderheide RH, Smyth EM. Mammary carcinoma cell derived cyclooxygenase 2 suppresses tumor immune surveillance by enhancing intratumoral immune checkpoint activity. *Breast Cancer Res*. 2013;15(5):R75.
67. Markosyan N, et al. Deletion of cyclooxygenase 2 in mouse mammary epithelial cells delays breast cancer onset through augmentation of type 1 immune responses in tumors. *Carcinogenesis*. 2011;32(10):1441–1449.
68. Zelenay S, et al. Cyclooxygenase-dependent tumor growth through evasion of immunity. *Cell*. 2015;162(6):1257–1270.
69. Böttcher JP, et al. NK cells stimulate recruitment of cDC1 into the tumor microenvironment promoting cancer immune control. *Cell*. 2018;172(5):1022–1037.e14.
70. Philip B, et al. A high-fat diet activates oncogenic Kras and COX2 to induce development of pancreatic ductal adenocarcinoma in mice. *Gastroenterology*. 2013;145(6):1449–1458.
71. Funahashi H, et al. Delayed progression of pancreatic intraepithelial neoplasia in a conditional Kras(G12D) mouse model by a selective cyclooxygenase-2 inhibitor. *Cancer Res*. 2007;67(15):7068–7071.
72. Hill R, et al. Cell intrinsic role of COX-2 in pancreatic cancer development. *Mol Cancer Ther*. 2012;11(10):2127–2137.
73. Müller-Decker K, et al. Preinvasive duct-derived neoplasms in pancreas of keratin 5-promoter cyclooxygenase-2 transgenic mice. *Gastroenterology*. 2006;130(7):2165–2178.
74. Hingorani SR, et al. Trp53R172H and KrasG12D cooperate to promote chromosomal instability and widely metastatic pancreatic ductal adenocarcinoma in mice. *Cancer Cell*. 2005;7(5):469–483.
75. Rhim AD, et al. EMT and dissemination precede pancreatic tumor formation. *Cell*. 2012; 148(1-2):349–361.
76. Wang D, et al. Cardiomyocyte cyclooxygenase-2 influences cardiac rhythm and function. *Proc Natl Acad Sci U S A*. 2009;106(18):7548–7552.
77. Yu Z, et al. Disruption of the 5-lipoxygenase pathway attenuates atherogenesis consequent to COX-2 deletion in mice. *Proc Natl Acad Sci U S A*. 2012;109(17):6727–6732.
78. Beatty GL, et al. CD40 agonists alter tumor stroma and show efficacy against pancreatic carcinoma in mice and humans. *Science*. 2011;331(6024):1612–1616.
79. Gunderson AJ, et al. Bruton tyrosine kinase-dependent immune cell cross-talk drives pancreas cancer. *Cancer Discov*. 2016;6(3):270–285.
80. Anaya J. OncoLnc: linking TCGA survival data to mRNAs, miRNAs, and lncRNAs. *PeerJ Computer Science*. 2016;2:e67.
81. Love MI, Huber W, Anders S. Moderated estimation of fold change and dispersion for RNA-Seq data with DESeq2. *Genome Biol*. 2014;15(12):550.
82. Patro R, Duggal G, Love MI, Irizarry RA, Kingsford C. Salmon provides fast and bias-aware quantification of transcript expression. *Nat Methods*. 2017;14(4):417–419.
83. Heinz S, et al. Simple combinations of lineage-determining transcription factors prime cis-regulatory elements required for macrophage and B cell identities. *Mol Cell*. 2010;38(4):576–589.
84. Sanjana NE, Shalem O, Zhang F. Improved vectors and genome-wide libraries for CRISPR screening. *Nat Methods*. 2014;11(8):783–784.
85. Yousefzadeh MJ, et al. Mechanism of suppression of chromosomal instability by DNA polymerase POLQ. *PLoS Genet*. 2014;10(10):e1004654.